

Determining the evolution of dust formation in SN 1987A using line profile asymmetries

Antonia Bevan¹ and M. J. Barlow¹

¹*Department of Physics and Astronomy, University College London, Gower Street, London WC1E 6BT, UK*

Accepted

ABSTRACT

Unexpectedly large masses of dust up to $0.7M_{\odot}$ have been discovered in the ejecta of SN 1987A. These dust masses are based on fitting the observed mid-IR and far-IR continuum. Additionally, in many supernovae, line profiles in the optical and near-IR exhibit a red-blue asymmetry as a result of greater extinction to radiation emitted from the receding part of the supernova. We here present a new code, DAMOCLES, that models the effects of dust on line profiles of core-collapse supernovae in order to determine masses of newly formed dust. We have tested the code against previously published models and against analytical results. We discover that the presence of a shoulder near the peak or an extended red scattering wing in line profiles may be suggestive of dust formation. We also note that dust-affected line profiles need not necessarily be asymmetrically oriented towards to the blue, although the peak must be blue-shifted. We have collated optical spectra from a variety of archives and modelled the evolution of the H α line from day 714 to day 3604. We also present models of the blue-shifted [OI] λ 6300,6363Å doublet at days 714 and 806. We conclude that a significant dust mass ($\sim 0.1M_{\odot}$) may have formed by day 3604 and infer that the majority of the dust mass must form after this epoch. For pure amorphous carbon models, large grain sizes ($\geq 0.6\mu\text{m}$) capable of surviving the reverse shock are required to fit the data even at very early epochs (day 714). Our findings are in strong agreement with previous SED models and confirm the suggestion that the majority of dust forms many years after the initial explosion when most supernovae are no longer detectable in the mid-IR.

Key words: supernovae: general - supernovae: individual: SN 1987A - ISM: supernova remnants - radiative transfer

1 INTRODUCTION

Core-collapse supernovae have long been thought to be potential dust factories. Over the past decade, observations in the IR have suggested that the quantities of dust produced are too low to account for the masses measured in the early universe. However, recent Herschel and Planck far-IR and sub-mm observations of massive dust reservoirs (as high as $0.7M_{\odot}$) have resulted in a reevaluation of the rate of dust production in these objects (Barlow et al. 2010; Gomez et al. 2012) [mikako ref problem]. These estimates are based on fitting the observed mid-IR and far-IR continuum. Following the end of the Herschel mission in April 2013 there is now a long wait for comparable or better spaceborne thermal IR facilities to become available, with the next major IR mission SPICA not due to launch until 2022. However, insight may still be gained via other means.

The absorption and scattering of optical or near-IR radiation by newly-formed dust within the ejecta of supernovae can result in an asymmetry between the red and blue

shifted components, with redwards emission from the far side of the ejecta undergoing greater absorption. Lucy et al. (1989) identified a line asymmetry in the 6300 Å [OI] line from SN1987A between 5 August 1989 and 3 March 1989, where the later spectrum was blue-shifted by $\sim 600\text{km s}^{-1}$. Since then, such red-blue asymmetries have been frequently observed in the late-time ($t > 400\text{d}$) spectra of supernova ejecta and there is a large database of these observations available (reference problem).

SN 1987A is an object that is not only fascinating but critical to our growing understanding of the formation and evolution of dust in core collapse supernovae. There have been numerous observations at all wavelength ranges and at all epochs. Blue-shifted lines are frequently observed in the spectrum. It has been deduced that very large masses of dust have formed within the ejecta of SN 1987A [mikako ref problem] but until recently the rate of dust formation in this object had been unclear. Recent modelling by Wesson et al. (2015) (hereafter W15) has provided some of the first

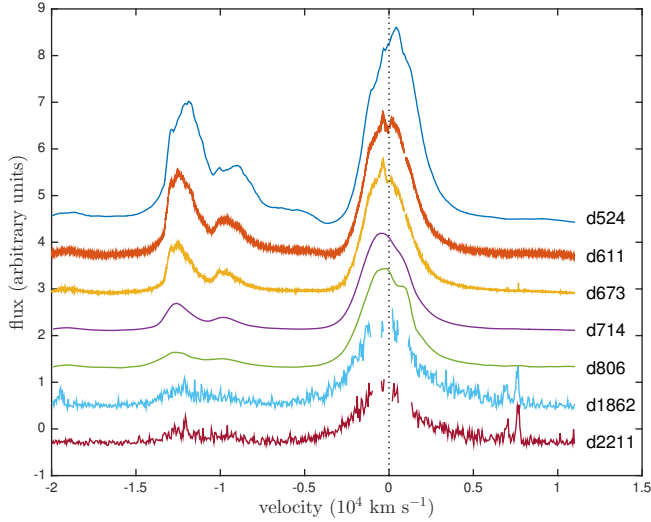


Figure 1. Archival data showing the evolution of the H α line from SN 1987A at early epochs with narrow line emission from the ring removed

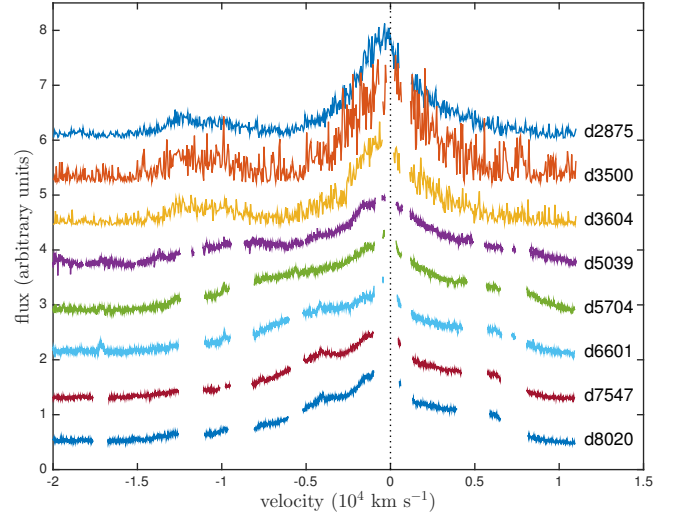


Figure 2. Archival data showing the evolution of the H α line from SN 1987A at late epochs with narrow line emission from the ring removed

clear insights into the rate of dust formation in the ejecta of SN 1987A.

We here seek to model formally the effects of dust on line profiles with a view to providing both an alternative methodology for determining dust masses formed in the ejecta of core-collapse supernovae and to investigate the potential effects of dust on the shape of line profiles emitted from these objects. We present a new code, DAMOCLES (Dust Affected Models Of Characteristic Line Emission in Supernovae), that utilises a Monte Carlo methodology in order to radiatively model line profiles in expanding atmospheres. The code allows for dust to be composed of multiple species and grain sizes with variable density and velocity distributions. Both clumped and smooth geometries may be modelled.

In this paper we collate optical spectra from the archives of four different telescopes in order to study the effects of dust formation on the H α line and the [OI] λ 6300,6363Å doublet. We model five different epochs spanning a range of approximately 8 years from the first indications of blue-shifting in the H α line at \sim day 700 using both smooth and clumped geometries. We compare the derived dust masses to those obtained by W15 and consider the implied formation rate. We present our testing of the new code against analytical cases and previously published optically thick models from the literature (Lucy et al. 1989). We also present our investigation into the sensitivity of each of the various variable parameters and consequently note the signatures that observed line profiles may exhibit in the presence of dust.

In section 2 we detail the spectra that we obtained for our modelling. In section 3 we discuss the details of the DAMOCLES code and we present our testing of the code and our parameter sensitivity analyses in section 4. Our modelling of the H α and [OI] λ 6300,6363Å lines is presented in section 5 and finally we discuss our findings in section 6.

2 ARCHIVAL SPECTRA OF SN 1987A

SN 1987A is one of the most observed objects in history and there is a wealth of both spectral and photometric data available to model. We have here collated optical and infra-red (IR) spectra from the archives of a number of different instruments over a wide range of epochs covering the majority of the lifetime of this object. At early epochs we use data obtained from the Anglo-Australian Telescope (AAT) and Cerro Tololo Inter-American Observatory (CTIO) archives and at later epochs spectra from the Hubble Space Telescope (HST) and Very Large Telescope (VLT) archives. An explosion date of 23 February 1987 is assumed throughout and all ages are measured relative to this date. Full details of all observations may be found in Table 1.

Wavelength ranges encompassing the H α line and [OI] λ 6300,6363Å doublet were selected in order to trace their evolution from around the time of the first indications of dust formation (day 524) to the current era (day 8020). Optical spectroscopy obtained at the AAT using the Faint Object Red Spectrograph (FORS) during the first two years was kindly supplied by Dr Raylee Stathakis (Spyromilio et al. 1991, 1993; Hanuschik et al. 1993) and all other spectra were obtained from online archives.

The evolution of the H α line is presented in figures 1 and 2. At later epochs, the broad profile emitted by the ejecta becomes contaminated by narrow line emission from the ring. These lines have been removed for the purposes of modelling the broad line. The continuum has been subtracted for each spectrum assuming a flat continuum level determined by the flux in the velocity ranges detailed in table 2. The spectra are scaled to unity at $v = -1800 \text{ km s}^{-1}$ and are offset from each other by 0.8. A recession velocity of 287 km s^{-1} is adopted (Grönningsson et al. 2008).

Table 1. Details of the archival data for SN 1987A

Date	Age (days)	Telescope	Inst	λ_{min} (Å)	λ_{max} (Å)	Res. (Å)	Res. Power	Reference
31 Jul 1988	524	AAT	FORS	5500	10190	20		Spyromilio et al. (1991)
26 Oct 1988	611	AAT	UCLES	6011	7336		30000	Hanuschik et al. (1993); Spyromilio et al. (1993)
27 Dec 1988	673	AAT	UCLES	5702	10190		30000	Hanuschik et al. (1993); Spyromilio et al. (1993)
06 Feb 1989	714	CTIO-1.5m	Cass.	6420	10380	16		Phillips et al. (1990)
09 May 1989	806	CTIO-1.5m	Cass.	6430	10330	16		Phillips et al. (1990)
30 Mar 1992	1862	HST	STIS	4569	6818	4.379		Wang et al. (1996)
14 Mar 1993	2211	HST	STIS	4569	6818	4.379		Wang et al. (1996)
07 Jan 1995	2875	HST	STIS	4569	6818	4.379		Chugai et al. (1997)
23 Sep 1996	3500	HST	STIS	4569	6818	4.379		
05 Jan 1997	3604	HST	STIS	4569	6818	4.379		
10 Dec 2000	5039	VLT	UVES	4760	6840		50000	Gröningsson et al. (2006, 2007)
06 Oct 2002	5704	VLT	UVES	4760	6840		50000	Gröningsson et al. (2006, 2007, 2008)
21 Mar 2005	6601	VLT	UVES	4760	6840		50000	Gröningsson et al. (2006, 2007)
23 Oct 2007	7547	VLT	UVES	4760	6840		50000	Gröningsson et al. (2007)
07 Feb 2009	8020	VLT	UVES	4800	6800		50000	Tziamtzis et al. (2010)

Table 2. Details of the adopted continuum levels at all epochs for SN 1987A

Epoch (days)	Velocity Range km s ⁻¹	Continuum Level (ergs cm ⁻² s ⁻¹ Å ⁻¹)
524	11000 - 17000	3×10^{-13}
611	15000 - 20000	7×10^{-14}
673	15000 - 20000	3×10^{-14}
714	15000 - 20000	2×10^{-14}
806	15000 - 20000	8×10^{-15}
1862	9000 - 11000	7×10^{-17}
2211	9000 - 11000	6×10^{-17}
2875	9000 - 11000	2×10^{-17}
3500	9000 - 11000	8×10^{-18}
3604	9000 - 11000	9×10^{-18}
5039	-20000 - -15000	4×10^{-17}
5704	-20000 - -15000	6×10^{-17}
6601	-20000 - -15000	7×10^{-17}
7547	-20000 - -15000	1×10^{-16}
8020	-20000 - -15000	1×10^{-16}

3 DESCRIPTION OF THE DAMOCLES CODE

Monte Carlo methods have long been used to model radiative transfer problems in diverse environments and there are several examples of codes which utilise the technique in application to supernovae (*references*). Whilst there are numerous instances of these codes treating either dust or gas or both in order to produce an overall spectral energy distribution (SED), there is seemingly a dearth of codes that are designed to focus on the shape of a single line profile. Codes that look to reproduce the spectra of supernovae generally utilise the Sobolev approximation in order to process the evolution of a series of line profiles and, though a velocity field is naturally considered, dust absorption and scattering is not and thus the resulting shapes of line profiles are potentially unrepresentative of those produced in dusty regions.

In this work we aim to model a single line profile or doublet produced by a moving atmosphere in a dusty medium. Since a comparatively small wavelength range is considered, a fully self-consistent radiative transfer model is unnecessarily expensive. Instead any packet that is absorbed during the simulation may simply be removed from circulation on the grounds that it would be reemitted outside the wavelength range of interest. Extinction due to dust is also temperature-

independent and it is therefore unnecessary to iteratively calculate the temperature of the ejecta as in a fully self-consistent calculation of the SED. Though clearly the total energy transferred through the medium is not conserved, the signature of the normalised line profile is preserved.

The DAMOCLES code builds on the work of Lucy et al. (1989) who employed a similar approach to model the broad [O] $\lambda 6300\text{\AA}$ line seen in SN 1987A at early epochs (\sim day 775). It models the transport of initially monochromatic energy packets through a smooth or clumped medium of dust in a smooth velocity field.

3.1 The energy packets formalism

The initial radiation field is inherently tied to the distribution of gas throughout the supernova ejecta which is declared as a power law $\rho(r) \propto r^{-\beta}$ between R_{in} and R_{out} . The emissivity distribution is also specified as a power law with $i(\rho) \propto \rho^k$. However this is generally taken to be $i(r) \propto r^{-2\beta}$ since the majority of lines modelled are recombination lines and therefore $i(\rho) \propto \rho^2$. The radiation is quantised into monochromatic packets with equal energy $E_0 = nh\nu_0$. In Monte Carlo simulations that model non-moving atmospheres, packets are usually taken to be of constant energy. When the frequency of a packet is altered after an event, the energy of that packet is kept constant and the number of real photons contained within it assumed to change. However, in the case of dust scattering, the number of real photons is conserved and thus the energy of the packet is altered. This is most easily achieved by weighting each packet over all scattering events as

$$w = \prod_{scat} \frac{\nu'}{\nu}$$

where w is the weight of the packet. The final energy of each packet is then $E = wE_0$, where E_0 is the initial energy of the packet.

The supernova ejecta is divided into shells between R_{in} and R_{out} and the number of packets to be emitted in each shell calculated according to the emissivity distribution and emitted isotropically. For each packet a location within that

shell and an initial trajectory is randomly sampled from an isotropic distribution such that

$$\phi = 2\pi\eta \implies \cos\theta = 2\xi - 1 \quad (1)$$

where $0 < \eta < 1$ and $0 < \xi < 1$ are random numbers, ϕ is the azimuthal angle and $\cos\theta$ is the radial direction cosine. At emission and at each scattering event the frequency of the packet is recalculated according to the specified radial velocity field $v(r) \propto v_{max}r^\alpha$ (see section 3.3).

3.2 The geometry of the ejecta and the grid

The supernova ejecta is approximated by a three-dimensional cartesian grid, each cell of which is assumed to have uniform density and composition. The grid is a cube with sides of width $2R_{out}$ and a declarable number of divisions. After the initial emission of energy packets, the gas plays no further role in the simulation and thus only dust properties are considered. By default, the dust is coupled to the gas (although it may be decoupled) and thus follows the smooth distribution described above ($\rho \propto r^{-\beta}$). The dust density in each cell is therefore calculated accordingly and any cell whose centre falls outside of the bounds of the supernova ejecta has density set to zero.

It is worth noting that if a constant mass loss rate is required, the exponent of the velocity profile and the exponent of the density profile are not independent. A constant mass loss rate implies that $4\pi\rho vR^2 \propto k$, where k is a constant, and thus for $v \propto r^\alpha$ and $\rho \propto r^{-\beta}$, we require that $\beta - \alpha = 2$. However, it is possible that the supernova event may have induced a mass-flow rate that is not constant with radius and thus both exponents may be declared independently.

It is known from SED modelling that clumped environments produce very different results to environments assumed to have a smooth distribution of dust and gas. Specifically, clumped models tend to require more dust in order to reproduce a similar level to a smoothly distributed model. The capacity for modelling a clumped dusty medium is therefore included in the code. The fraction of the dust mass that is in clumps is declared (m_{frac}) and the total volume filling factor of the clumps (f) is also specified. Dust that is not located in clumps is distributed according to a smooth radial profile. The clumps occupy a single grid cell and their size can therefore be varied by altering the number of divisions in the grid. They are distributed stochastically with probability of a given cell being a clump proportional to the smooth density profile (i.e. $p(r) \propto r^{-\beta}$). The density of all clumps is constant and is calculated as

$$\rho_{clump} = \frac{M_{clumps}}{V_{clumps}} = \frac{m_{frac}M_{tot}}{\frac{4}{3}f\pi(R_{out}^3 - R_{in}^3)} \quad (2)$$

where M_{tot} is the total dust mass, M_{clumps} is the total dust mass in clumps and V_{clumps} is the total volume occupied by clumps. m_{frac} and f are defined as above.

3.3 The radiative transport mechanism

Following emission a packet must be propagated through the grid until it escapes the outer bound of the ejecta R_{out} .

The probability that the packet travels a distance l without interacting is $p(l) = e^{-n\sigma l} = e^{-\tau}$ where n is the number density, σ is the cross-section of interaction and $\tau = n\sigma l$ for constant n and σ (as in a grid cell). Noting that the probability that a packet does interact within a distance l is therefore $1 - e^{-\tau}$, we may sample from the cumulative probability distribution to give:

$$\xi = 1 - e^{-\tau} \implies \tau = -\log(1 - \xi) \quad (3)$$

where $0 < \xi < 1$ is a sampled random number set to be the value of the optical depth for that packet in that cell. The frequency of the photon packet and the mass density of the cell are then used to calculate the opacity of that cell and, using the fact that $n\sigma = \kappa\rho$, the distance l that the packet travels before its next interaction is calculated. If this value is greater than the distance from its position to the edge of the cell then the packet is moved along its current trajectory to the cell boundary and the process is repeated. If the distance is less than the distance to the boundary then an event occurs and the packet is either scattered or absorbed with probability of scattering equal to the albedo of the cell

$$\omega = \frac{\sigma_{sca}}{\sigma_{sca} + \sigma_{abs}} \quad (4)$$

If the packet is absorbed then it is simply removed from the simulation as discussed above. If the packet is scattered then a new trajectory is sampled from an isotropic distribution in the comoving frame of the dust grain and the frequency of the packet recalculated using Lorentz transforms subject to the velocity at the radius of the interaction (see appendix A for further details). This process is repeated until the packet has either escaped the outer bound of the supernova ejecta or been absorbed.

Escaped packets are added to frequency bins weighted by w in order to produce an overall emergent line profile.

3.4 Properties of the Dusty Medium

Dust of any composition may be used for which optical data is available and the relative abundances of the species may be declared by the user. A grain size may be specified for each species. Since a full radiative transfer calculation is not performed, it is not useful to specify a grain size distribution since the extinction to dust is only dependent on the cross-sectional area of the grains and not to the overall distribution. The capacity to declare a size distribution is however included for the sake of ease of comparison with SED models. A Mie approximation is used to calculate the overall $Q_{abs}(\nu)$ and $Q_{sca}(\nu)$ for each species and the derived opacities are summed over each species weighted according to their relative abundances.

As will be discussed in sections 4, the effects of scattering on the shapes of line profiles can potentially be quite pronounced and it is therefore important to consider the potential effects of electron scattering as well as those of dust scattering. Electron densities are calculated using an estimated average temperature and observed luminosity of H_α and the optical depth to electrons calculated from this. Electron scattering is treated in an identical manner to dust

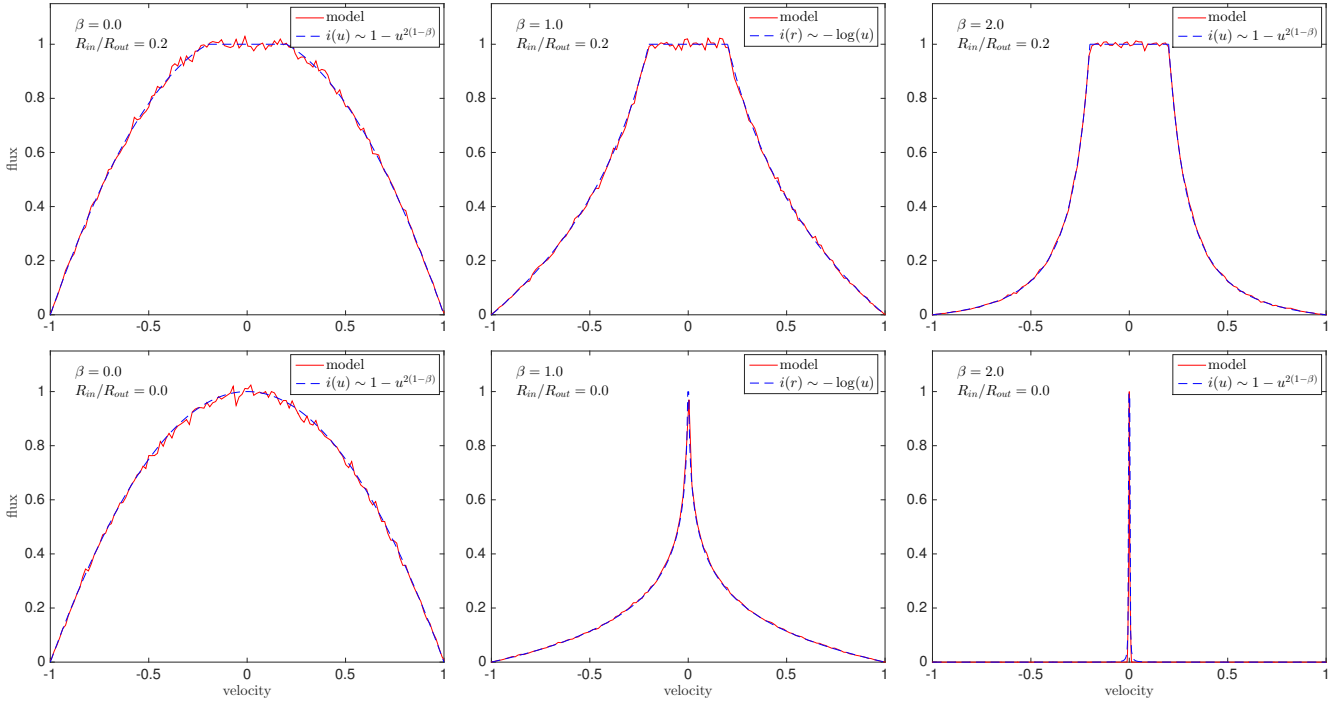


Figure 3. Red: Benchmark models of optically thin ($\tau = 0$) line profiles with $v \propto r$. Left to right: initial emissivity profiles are $i(r) \propto r^{-2\beta}$ with $\beta = 0.0$, $\beta = 1.0$ and $\beta = 2.0$. Cases with $R_{in}/R_{out} = 0.2$ are on the top and $R_{in}/R_{out} = 0.0$ on the bottom. Blue: The analytical case with $i(u) \sim 1 - u^{2(1-\beta)}$ except in the case of $\beta = 1$ where $i(u) \sim -\log u$.

scattering with $\tau = \tau_{dust} + \tau_e$ in each cell. If, for a given packet, an event occurs, it is first calculated whether this is a dust event or a scattering event by considering the ratio of the optical depths to each species. If the packet is scattered by an electron then this process is identical to dust. If not, then the process continues as described above.

In the majority of cases it seems that the electron densities are not high enough to discernibly effect the overall shape of the profile. However, there may be a few rare cases (the concept is discussed for SN 2010jl (Fransson et al. 2013)) where the electron densities are high enough to become significant in the observed profiles. Whilst the inclusion of electron scattering in the code is an approximation, it gives a good suggestion of the potential effects of electron scattering.

4 COMPARISON OF DAMOCLES MODELS WITH ANALYTICAL AND PREVIOUSLY PUBLISHED RESULTS

There is a general lack of published models in the literature that consider absorption-affected asymmetric line profiles. We therefore test the code by comparing the results to optically thin profiles that may be derived analytically. We then test the absorption and scattering components of the code by comparing our results in the case of an optically thick medium with those derived by Lucy et al. (1989) in their Model II and Model III scenario.

4.1 Comparison of DAMOCLES models with analytical results

Analytical profiles may be calculated in the dust-free case. I run a number of models based on mathematics derived by Gerasimovic (1933) that derive the equations of line profiles emitted from a transparent expanding shell in the field of a star.

Describing the expansion velocity of the shell as $v = r^\alpha$ with $\alpha \neq 0$ and maximum velocity $v_{max} = 1$, the energy emitted by the nebula between radial velocities v and $v + dv$ is proportional to

$$\int_{\tau} i(r) r \sin(\theta) r d\theta dr \quad (5)$$

where $i(r)$ represents the emission per unit volume at radius r . We adopt inner radius $R = q$ and outer radius $R = 1$.

Setting $i(r) \propto r^{-2\beta}$ (for a recombination line emitted from a medium with assumed density profile for the emitter $\rho \propto r^{-\beta}$) then gives

$$\begin{aligned} i(v)dv &\sim \frac{dv}{\alpha v^{\frac{2\beta-3+\alpha}{\alpha}}} \int_{\theta_0}^{\theta_1} \cos^{\frac{2\beta-3}{\alpha}} \theta \sin \theta d\theta \\ &\sim \frac{dv}{v^{\frac{2\beta-3+\alpha}{\alpha}}} \left[\frac{\cos^{\frac{2\beta-3+\alpha}{\alpha}} \theta}{2\beta-3+\alpha} \right]_{\theta_1}^{\theta_0} \end{aligned} \quad (6)$$

for $\frac{2\beta-3}{\alpha} \neq -1$. The case $\frac{2\beta-3}{\alpha} = -1$ results in a logarithmic relationship.

In the case of a "complete" nebula, i.e. one where the

inner radius is vanishingly small in comparison to the outer radius, we obtain

$$i(v)dv \sim \pm \frac{du}{(2\beta - 3 + \alpha)v^{\frac{2\beta-1+\alpha}{\alpha}}} \left(1 - v^{\frac{2\beta-3+\alpha}{\alpha}}\right) \quad (7)$$

If the nebula is not "complete", that is to say, the inner radius is of the order of the outer radius and the remnant is a detached shell, the above formula becomes valid only from $v = 1$ to some critical value $v' = q^\alpha$. For $v < v'$, we obtain

$$i(v)dv \sim \pm \frac{dv}{(2\beta - 3 + \alpha)} \left(\frac{1}{q^\alpha} - 1\right) \quad (8)$$

and therefore the top of the line is flat while the sides are sloping.

Crucially, the width of the flat section is determined by $v' = q^\alpha$ or simply $v' = q$ in the case where $v \propto r$, whilst the shape of the profile outside of the flattop is described by equation 7.

Profiles of a variety of shapes may be derived from these formulae depending on the relative values of α and β . Here we consider three main families of curves:

- (i) $i(v) \sim v^{-\gamma} - 1$ ($\alpha > 0$, $2\beta - 3 + \alpha > 0$)
- (ii) $i(v) \sim 1 - v^\gamma$ ($\alpha > 0$, $2\beta - 3 + \alpha < 0$)
- (iii) $i(v) \sim -\log v$ ($\alpha > 0$, $2\beta - 3 + \alpha = 0$)

where γ is defined as $\gamma = \left|\frac{2\beta-3+\alpha}{\alpha}\right|$.

Models are presented for each of these cases, both in the environment of a complete nebula and one with a shell structure with $R_{in}/R_{out} = 0.2$. A velocity profile $v \propto r$ appropriate for a supernova in the free expansion phase is used throughout. Values of $\beta = 0, 1$ and 2 are adopted. Figure 3 illustrates the perfect fit between the analytical case and the model. Fluxes are scaled to 1 at the peak.

4.2 Comparison of DAMOCLES models with previously published results

In addition to the optically thin testing described above, we also compared our outputs to those derived by Lucy et al. (1989) in order to assess the accuracy of the scattering and absorption aspects of the code. We consider two similar cases equivalent to Models II and III in the Lucy et al. (1989) paper. In the first case, dust with zero albedo is uniformly distributed throughout a complete nebula with velocity profile $v \propto r$. In the second, the same scenario is considered but a medium of dust with $\omega = 0.6$ is considered.

In the first case, the profile may once again be derived analytically from the basic geometry using the fact that radiation will be attenuated by a factor $e^{-2\tau v}$ between points with line of sight velocity $-v$ and v . The line profile is therefore given by

$$I(v) = I(-v) \exp(-2\tau v)$$

Lucy et al. (1989) present several examples of both the analytical case of the perfect absorber and a Monte Carlo model for a grain with $\omega = 0.6$. We present the same cases in figure 4 and note that the resulting profiles exhibit the same features and shape. Of particular interest is the scattering

wing that appears beyond the maximum velocity ($v_{max} = 1$) on the red side of profiles in the case of the partial scatterer as a result of the packets doing work on the expanding sphere. This is noted by Lucy et al. (1989) as a potential diagnostic for the presence of dust in the ejecta of a supernova and we will discuss this further in section 4.3.

4.3 The sensitivity of the variable parameters

It is of general interest to establish potential diagnostic signatures in the profiles of supernovae and their remnants in order to trace dust formation more effectively. We here discuss the effects of the main parameters of interest, namely:

- v_{max}
- R_{in}/R_{out}
- β , where $\rho \propto r^{-\beta}$
- albedo ω
- optical depth τ

4.3.1 v_{max}

The maximum velocity is defined as the velocity at the very outer edges of the line emitting region for a given line. Note therefore that the maximum velocity may vary between different spectral lines or doublets due to the location of a particular species or differing ionization thresholds. Clearly, the larger the maximum velocity used the wider the profile becomes. To some extent therefore the incline of the density profile and the maximum velocity act to counter each other since a steeper density profile narrows the profile (see section 4.3.5). The shape of the wings of the profiles, however, generally preclude much degeneracy in this aspect - the overall shape of the line profile determines the exponent of the density profile to within a relatively small range.

More important is the effect that the maximum velocity has on the overall optical depth. Since the overall volume of the ejecta is determined solely by the maximum velocity and the ratio of the inner and outer radii, the total optical depth to which the radiation is exposed is greatly affected by even a relatively small change in the maximum velocity. Practically speaking, the maximum velocity may be fairly well determined from the observations (as identified as the point where the flux vanished on the blue side) and may be further constrained through modelling.

4.3.2 R_{in}/R_{out}

As already discussed in section 4.1, the width of the flat top may be determined solely by the ratio of the inner and outer radii, the exponent of the velocity profile and the maximum velocity. It is valid to assume that the velocity profile takes the form $v \propto r$ even from just a few months after the explosion as the supernova is in free expansion. This means that R_{in}/R_{out} may be calculated as

$$\frac{R_{in}}{R_{out}} = \frac{v_{min}}{v_{max}}$$

where it is often possible to constrain v_{min} and v_{max} to a relatively narrow range simply from the observed line profile.

The majority of spectral lines emitted from supernovae

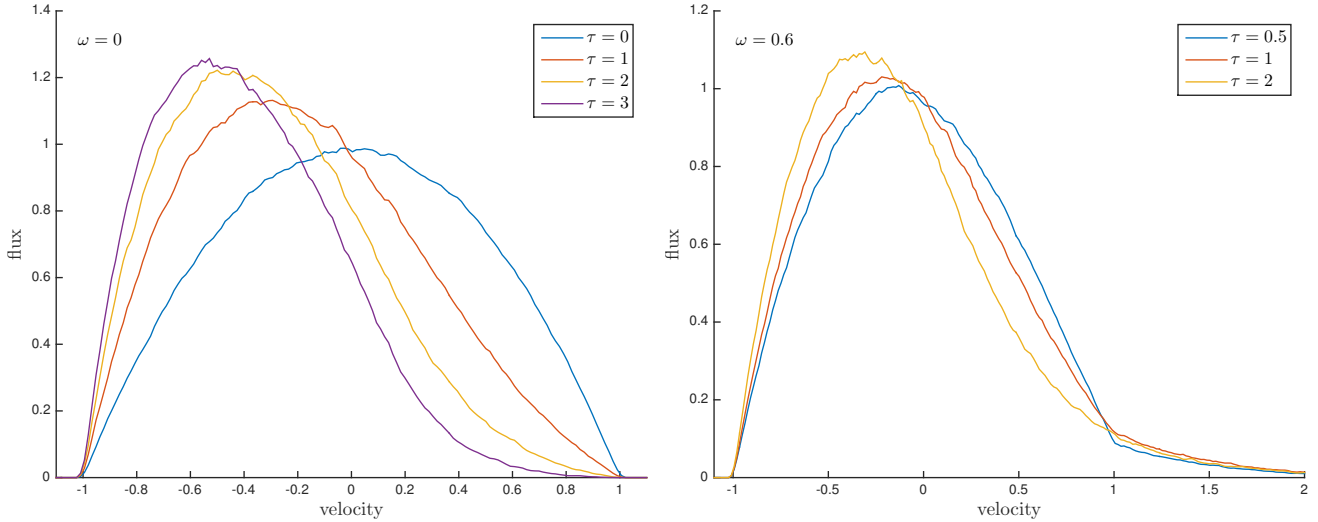


Figure 4. Benchmark models of optically thick line profiles with $v \propto r$, $i(r) \propto \text{constant}$ and $R_{in}/R_{out} = 0$. Pure absorption models ($\omega = 0$) are presented on the left, partially scattering models are presented on the right ($\omega = 0.6$) as per Lucy et al. (1989) Models II and III.

and supernova remnants would be expected to have a flat top since it is rare for these objects to form a complete nebula. However, even a very small amount of attenuation may result in the profile appearing to be more smoothed at its peak.

The effect on the line profile of adopting $R_{in}/R_{out} = 0$ as opposed to a detached shell may be seen in figure 3.

4.3.3 τ

As expected, greater attenuation of the original line profile is seen on the red side than on the blue. The profiles are most revealing at lower optical depths. The affects of the asymmetric absorption can be seen in different sections of the profiles. The region of the profile that is most clearly affected by dust absorption is the flat-topped region. A small amount of absorption in this region results in a skewed profile, with a fraction of the flat-topped section removed. The peak becomes blue-shifted as a result, but only to the original value of the minimum velocity of the profile. In addition to the attenuation in this region, the red wing of the profile is also somewhat reduced, and the blue wing somewhat increased relative to their original symmetric positions. The result is a relatively ‘jagged’ looking profile, often with sharp changes at $\pm v_{min}$. The profile is generally asymmetric, although the degree of absorption in the flat-topped region may sometimes make it seem as though the profile is in fact symmetric and uniformly blue-shifted (see section 4.5 for further discussion).

At high optical depths the entire profile is shifted to the blue and the peak moves beyond the minimum velocity further into the blue. The profiles also become more smoothed. A full set of models investigating the effects of varying optical depths under different density profiles and albedos are presented in figures 5 and 6.

4.3.4 ω

In the past, focus has largely been on the effects of absorption by dust on the shapes of line profiles and little attention has been paid to the potential effects of scattering by dust grains. In fact, line profiles are significantly affected by scattering of radiation. Not only does repeated scattering of photons increase the number of potential opportunities for a given photon to be absorbed but it also results in continuous shifting of the frequency of the photon to the red. The photon must do work on the expanding shell of dust in order to escape and thus many of the photons are reprocessed beyond the theoretical maximum velocity into the red side of the profile. The result is a substantial, extended wing on the red side of the line. In the case of strong scatterers, this can result in an asymmetric profile that is the reverse of that normally expected with the majority of the emission on the *red* side. The peak however, remains blue-shifted. See figure 6 for a full investigation of the variation of ω and τ .

The implications of this result in relation to the use of line profiles as a diagnostic for tracing dust formation in supernova ejecta are significant and are discussed further in section 4.5.

4.3.5 $\rho \propto r^{-2\beta}$

Whilst the density profile of the dust may have some effect on the resulting profiles, it is the initial emissivity profile (dependent on the dust density profile) that has greatest effect on the resulting shape of the line profile.

In general, the steeper the emissivity distribution, the narrower the line profile becomes. The sides of the line profile may become almost straight for a very steep distribution since the majority of the emission then comes from a very narrow velocity range. For a flat-topped profile of fixed width this approximates the square profile produced in the case of an emitting shell with constant velocity.

The dependence of the shape of the line profile in the

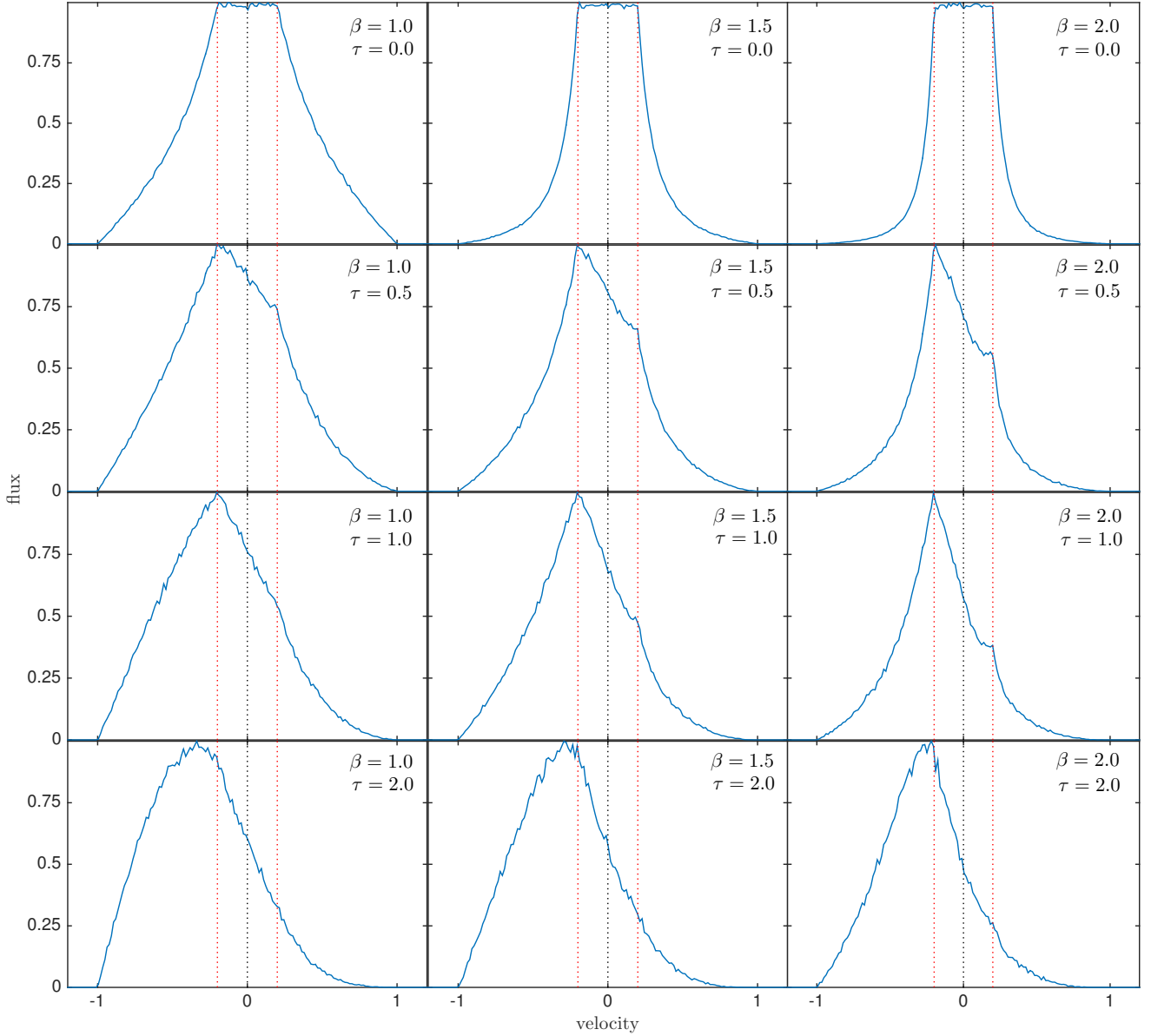


Figure 5. Set of models with $i(r) \propto r^{-2\beta}$, $\omega = 0$, $R_{in}/R_{out} = 0.2$ and $v_{max} = 1$ illustrating the effects of varying τ and ω . Maximum fluxes are scaled to 1.

optically thin case is described in section 4.1. However, the density profile also plays a significant role where there is even a small amount of absorption. As previously discussed, at relatively small optical depths, a section of the flat-topped region is removed resulting in a peak at $-v_{min}$. The shape of the profile in this region is significantly affected by the density profile. Shallow profiles produce a virtually linear variation in flux between $-v_{min}$ and $+v_{min}$. For a fixed optical depth, the steeper the distribution becomes, the more concave the profile becomes between $-v_{min}$ and $+v_{min}$, ultimately resulting in a clear shoulder to the profile at $+v_{min}$. For extremely steep distributions this ultimately results in a double peaked profile with the trough to the red of $v = 0$. A full investigation of the variation of β with τ is performed given in figure 5.

4.4 Inferring properties of the dust from the models

The presence of an extended red wing at large positive velocities in combination with increased extinction on this side at smaller positive velocities may allow for the values of τ and ω to be well constrained. In this case it is possible to translate these values into a dust mass and average grain size for a given species or combination of species using optical properties and a Mie approximation (see figure 7). In fact, it is the dust mass and average grain size that is varied within the code for a specified species or combination of species. It is therefore important to note that the use of different optical properties may substantially alter the produced optical depths and albedos for a given species of specific grain size as has been noted previously (Owen & Barlow 2015).

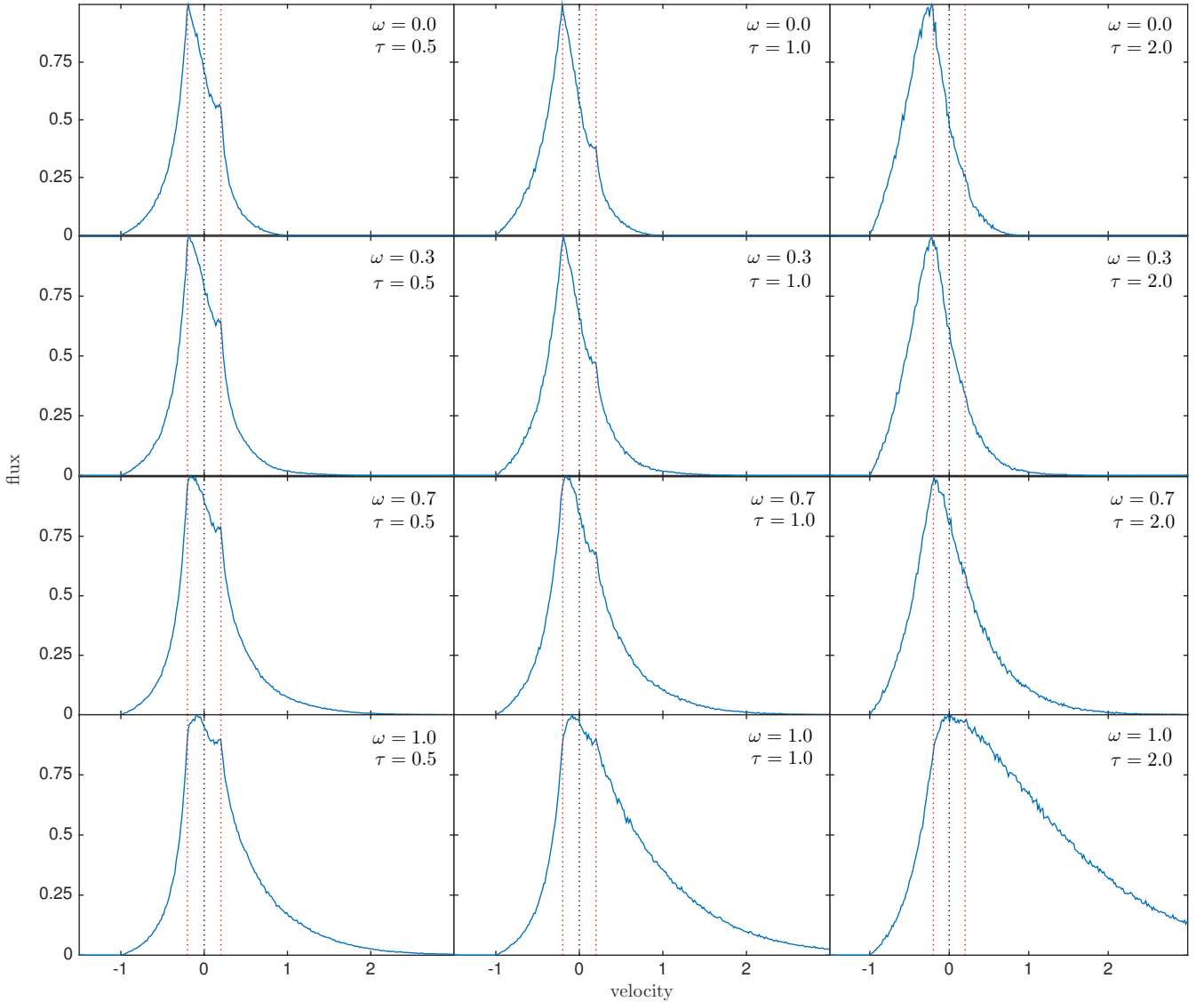


Figure 6. Set of models with $i(r) \propto r^{-4}$, $R_{in}/R_{out} = 0.2$ and $v_{max} = 1$ illustrating the effects of varying τ and ω . Maximum flux is scaled to 1.

For amorphous carbon, the larger the grain size used the larger the albedo and the smaller the cross-section of absorption. Larger masses of dust are therefore required to fit the same degree of absorption if a larger grain size is used. This is in contrast to SED radiative transfer modelling where larger grain sizes generally result in less dust being required to fit the IR portion of the SED (W15). These two techniques in tandem may therefore give excellent limits on grain sizes for specific species or combinations thereof.

4.5 Observable signatures of dust in line profiles

The greater the optical depth modelled, the more attenuation of the line is observed. As expected, the blue side of the profile suffers a greater degree of absorption than the red

side. The resulting asymmetry is somewhat more complex than perhaps previously thought however. Dust has repeatedly been cited as the agent responsible for the apparent blue-shifting of line profiles in supernovae in the manner of the profiles presented in figure 4. That is, relatively high optical depths result in an overall shift of the entire profile towards the blue.

In practice a relatively large optical depth ($\tau \approx 2$) is required to actively shift the peak of the profile beyond its natural minimum velocity. In most cases it seems more likely that the medium is in fact optically thin and the blue-shifting of the peak of the profile is likely a result of attenuation in the flat-topped section (close to R_{in}). The peak would therefore be located at $-v_{min}$.

Dust absorption is wavelength dependent. One might

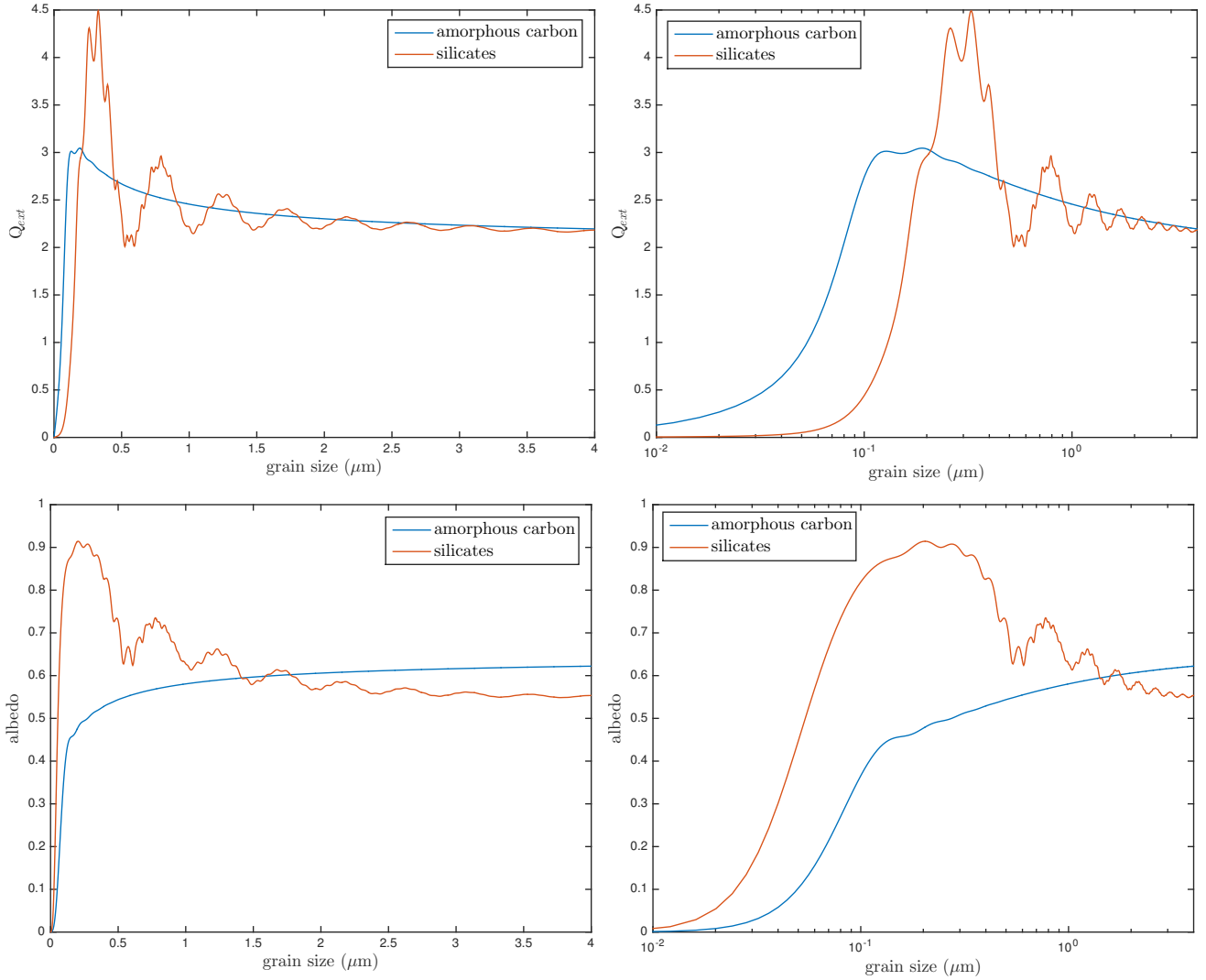


Figure 7. Variation of albedo with grain size for amorphous carbon and silicates sample using a Mie approximation at $\lambda = 658\mu\text{m}$. Optical constants from Zubko et al. (1996) and ?.

Table 3. Details of the parameters used for the best fitting smooth models with $a = 0.35\mu\text{m}$.

	day	v_{max} (kms^{-1})	R_{in}/R_{out}	β	M_{dust} (M_{\odot})	a (μm)	R_{out} (cm)	R_{in} (cm)	doublet ratio	$\tau_{H\alpha}$	τ_V	Figure No.
H α	714	3250	0.25	1.2	2.50E-05	0.35	2.00E+16	5.01E+15		0.61	1.23	Fig. 10
H α	806	4500	0.25	1.8	3.00E-05	0.35	3.13E+16	7.83E+15		0.30	0.60	Fig. 11
H α	1862	8500	0.15	1.9	6.00E-04	0.35	1.37E+17	2.05E+16		0.35	0.70	Fig. 12
H α	2875	9500	0.14	1.9	1.80E-03	0.35	2.36E+17	3.30E+16		0.36	0.72	Fig. 12
H α	3604	10250	0.13	1.9	5.00E-03	0.35	3.19E+17	4.15E+16		0.55	1.10	Fig. 12
[OI]	714	5000	0.17	2.8	9.50E-05	0.35	3.08E+16	5.24E+15	2.9	1.09	2.19	Fig. 10
[OI]	806	6000	0.15	2.7	1.60E-04	0.35	4.18E+16	6.27E+15	2.7	0.97	1.95	Fig. 11

therefore expect the position of the peak to be dependent on the wavelength of the line being considered. Indeed, the relationship between the locations of the peaks of profiles and their wavelength has been discussed by several authors in relation to dust formation (Gall et al. 2014; Fransson et al. 2013; Smith et al. 2012). We suggest here, that whilst this is likely the case in regions of high optical depth, this is not necessarily likely to be seen in the ejecta of most supernovae. The wavelength-dependence of dust absorption

instead results in differing degrees of extinction in the flat-topped region of each profile but leaves the peak at its blue-shifted position of $-v_{min}$. Of course, the value of v_{min} may be different for different species. However, if this is the case then there would be no reason to expect variation in the position of the peaks of profile to be correlated with the wavelength dependence of dust. Rather one would expect the location of the peak potentially to trace the location of elements within the ejecta. We demonstrate this dependence

for three lines, $H\alpha$ (6563Å), $H\beta$ (4861Å) and $Pa\delta$ (10049Å), in figure 8. We present the variation of the absorption cross-section with wavelength and illustrate the changes in the profiles for both optically thin and optically thick cases at three different grain sizes.

The attenuation of the flat-topped region is also often such that it may be very hard to discern a difference in slope between the attenuated section between $-v_{min}$ and $+v_{min}$ and the slope of the wing for $v > +v_{min}$, particularly in circumstances where data is of poor resolution or has a poor signal-to-noise ratio. Even in the case of excellent data, it may be easy to overlook these particular features or to dismiss them as natural fluctuations in the geometry of the ejecta. The possibility that they may be a product of dust formation should be considered.

The greater attenuation of radiation received from the receding portion of the ejecta results in an asymmetry of the line profile whereby the majority of emission is contained bluewards of the peak. However, there is an extent to which the effects of repeated scattering events within the ejecta serves to counter this asymmetry. Even in the case of dust grains with a relatively low albedo, a surprisingly persistent wing on the red side of the profile is seen, often beyond the maximum theoretical velocity of the emitting region. For higher albedos this can actively result in a shift in the overall asymmetry of the profile, with the majority of the emission being emitted redwards of the peak, though the peak itself remains blue-shifted.

This effect is obviously analogous to that of electron scattering which also produces a significant red wing in line profiles (Hillier 1991; Auer & Blerkom 1972). This is an important consideration in both modelling and analysis of spectral line profiles. DAMOCLES has the capacity to include a basic electron scattering mechanism in order to assess the possibility that any observed red wing might be produced by electron scattering rather than dust scattering. The red wing observed in line profiles is an excellent diagnostic for determining the overall albedo and it is therefore important to establish whether the origins of this feature are electron or dust scattering or a combination of the two.

The combination of relatively low optical depths, initially flat-topped profiles, greater attenuation on the blue side with increased flux on the red side due to scattering results in a profile that, somewhat bizarrely, can often end up appearing almost symmetrical, particularly if contaminants such as narrow lines or blending with other broad lines are present or if the resolution of the data is poor. Obviously highly asymmetrical profiles are also observed, but the potential for apparently symmetrical profiles that appear to have been uniformly blue-shifted should be noted and analysed carefully (see figures 5 and 6 for examples of this).

5 RESULTS

We model the $H\alpha$ line at days 714, 806, 1862, 2875 and 3604 and the $[O I]\lambda 6300, 6363\text{\AA}$ doublet at days 714 and 806. After this epoch the profile begins to become dominated by emission from the reverse shock and the structure of the emitting region may no longer be approximated by a single shell model as we do here. We maintain a velocity profile $v = \frac{v_{max}}{R_{max}} r$ and treat the variable parameters listed in sec-

tion 4.3. Whilst the albedo and optical depth are not varied directly, they are altered by adjusting the dust mass, M_{dust} , and the grain size, a , which will together determine the albedo and optical depth via a Mie scattering approximation and the optical properties of the dust.

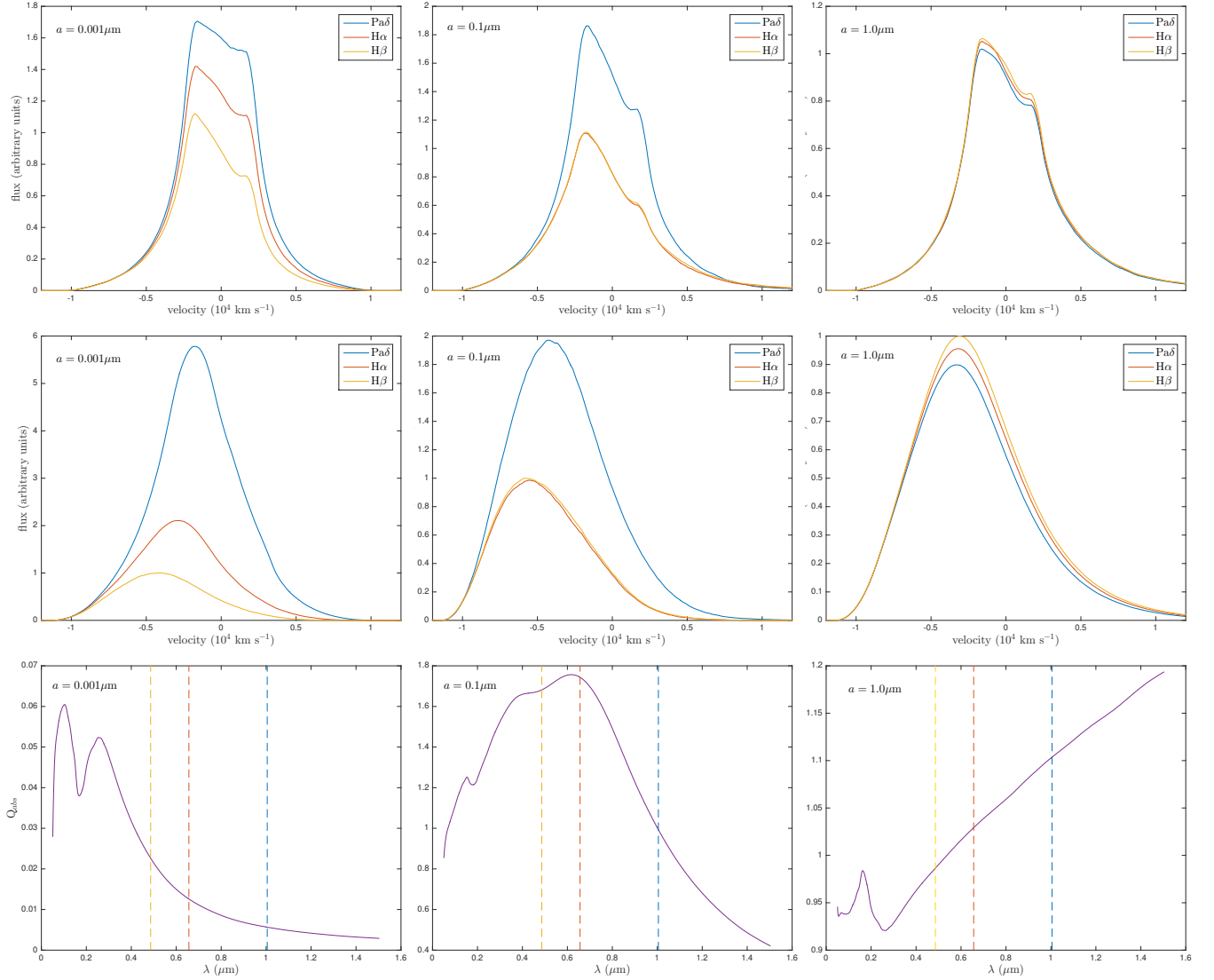
In all models, the ejecta occupies a shell with inner radius R_{in} and outer radius R_{out} . Packets are emitted according to a smooth density profile assuming recombination such that $i(r) \propto \rho(r)^2 \propto r^{-2\beta}$. Initially the dust is considered to have a smooth density distribution and is assumed to be coupled to the gas following the same radial profile. A clumped distribution of dust is considered later (see section 5.2). We do not include electron scattering in the code since the electron density is not high enough to affect the line profiles in any discernible fashion *references*.

As might be expected when fitting a single line with many variables, there is rarely a unique set of parameters that best fit the data. However, the majority of the parameters of interest may be well constrained by our modelling by considering different elements of the shape of the profile as we have previously discussed. In particular, by constructing good fits to the data using both conservative and optimistic estimates of the grain size, credible lower and upper bounds on the possible dust mass formed within the ejecta may be derived. We therefore present here a number of reasonable fits to the data using both small and large values of a since it is the grain size which has the most significant effect on the overall dust mass required to reproduce the profile (see section 4). We use an environment of pure amorphous carbon and use the optical constants from the BE sample presented in Zubko et al. (1996). Previous modelling has limited the fraction of silicates present in the dusty medium to a maximum of 15% (Wesson et al. 2015; Ercolano et al. 2007) and so an environment of pure amorphous carbon is likely to be reasonably representative of the true composition. If anything, pure amorphous carbon is the most conservative choice since the inclusion of even a small fraction of silicates is likely to increase the dust mass required.

For each profile, the maximum velocity is identified from the data as the point where the flux vanishes on the blue side. The equivalent point on the red side is indeterminate from observations due to the effects of scattering. Similarly, the 'corner' of the flat topped section of the profile on the blue side allows the minimum velocity at R_{in} to be ascertained. As discussed in section 4, this allows the ratio of the bounds of the supernova to be determined as $R_{in}/R_{out} = v_{min}/v_{max}$. The outer radius is calculated from the epoch and maximum velocity.

The only parameters that then remain to be determined are the exponent of the density profile β , the grain size and the dust mass. The shape of the blue wing is solely a product of the density profile and the dust mass; the height and shape of the red wing is a product of these and also of the scattering efficiency of the grains (the albedo ω); and the extent and shape of the asymmetry in the flat-topped portion of the profile is a result of only the total optical depth as determined by the dust mass and the grain size. By iterating over these three parameters therefore, an excellent fit to the data may be obtained.

Models are produced in the same manner for the $[O I]\lambda 6300, 6363\text{\AA}$ doublet as for a single line with each component of the doublet being modelled independently and

**Figure 8.** wavelength dependence**Table 4.** Details of the parameters used for the best fitting clumped models with $a = 0.6\mu\text{m}$.

	day	v_{max} (km s^{-1})	R_{in}/R_{out}	β	M_{dust} (M_{\odot})	a (μm)	R_{out} (cm)	R_{in} (cm)	doublet ratio	$\tau_{H\alpha}$	τ_V	Figure No.
H α	714	3250	0.25	1.2	7.00E-05	0.6	2.00E+16	5.01E+15		0.87	1.74	Fig. 13
H α	806	4250	0.25	1.9	1.00E-04	0.6	2.96E+16	7.40E+15		0.56	1.12	Fig. 14
H α	1862	8500	0.14	1.9	1.65E-03	0.6	1.37E+17	1.91E+16		0.48	0.96	Fig. 15
H α	2875	9500	0.12	2	1.00E-02	0.6	2.36E+17	2.83E+16		0.96	1.93	Fig. 15
H α	3604	10250	0.12	2	2.30E-02	0.6	3.19E+17	3.83E+16		1.21	2.42	Fig. 15
[OI]	714	5000	0.17	2.8	2.70E-04	0.6	3.08E+16	5.24E+15	2.6	1.02	2.03	Fig. 13
[OI]	806	6000	0.15	2.7	6.00E-04	0.6	4.18E+16	6.27E+15	2.4	1.66	3.32	Fig. 14

the resulting profiles added according to a specified ratio. Although the flux ratio is theoretically determined, the actual ratio between the two components is affected by self-absorption *reference* and it is therefore necessary to leave this as a free parameter. The [OI] $\lambda 6300, 6363\text{\AA}$ exhibits a clear blueshift as early as day 611 and provides another diagnostic for determining the dust mass allowing the wavelength dependence of dust absorption to be probed. By day

1862 the doublet is too blended and no longer strong enough to usefully model.

5.1 Smooth Models of SN 1987A

Even at the earliest epochs there is a substantial wing on the red side of the data that cannot be fitted with grains with a small albedo. The minimum required albedo is approxi-

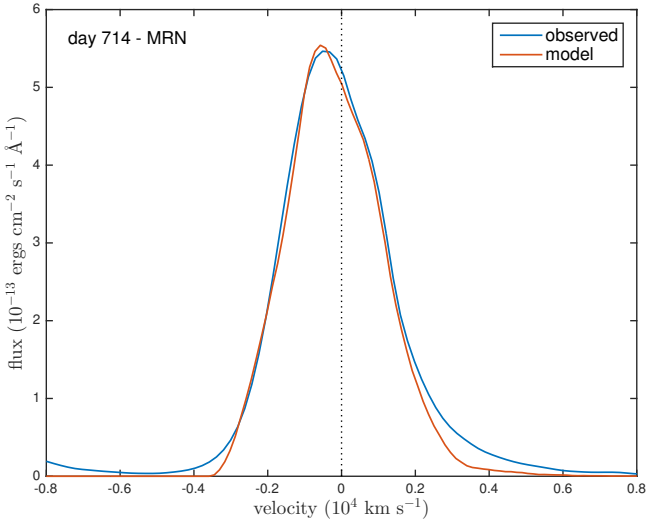


Figure 9. Conservative fit to the day 714 H α line illustrating the underestimation of the red scattering wing for small grain sizes. Model parameters are the same as the conservative fit to day 714 except for the grain size distribution and dust mass: $v_{max} = 3250 \text{ km s}^{-1}$, $R_{in}/R_{out} = 0.25$, $\beta = 1.2$, $M_{dust} = 8.0 \times 10^{-6} M_{\odot}$, $a_{min} = 0.005 \mu\text{m}$, $a_{max} = 0.25 \mu\text{m}$ and $n(a) \propto a^{-3.5}$.

mately $\omega \approx 0.5$. The larger the grain size the larger the mass of dust required to reproduce the same optical depth (since the optical depth is dependent only on the cross-sectional area of the grains). Figure 9 illustrates the best fit at day 714 in the case where the classical MRN grain size distribution is adopted with $a_{min} = 0.005 \mu\text{m}$, $a_{max} = 0.25 \mu\text{m}$ and $n(a) \propto a^{-3.5}$. It can be seen clearly that the red wing is significantly underestimated. Since the scattering efficiency of pure amorphous carbon varies significantly over a relatively small grain size range (see figure 7) we can establish a reasonably strong lower bound on the mean dust grain size, which we estimate to be approximately $a = 0.35 \mu\text{m}$. This is the smallest grain size that is still capable of reproducing the red scattering wing at all epochs and we therefore use this value throughout our smooth modelling.

The inner and outer radii are calculated at each epoch from the maximum velocity used, the day number and the specified ratio R_{in}/R_{out} . The radii generated are consistent with those used in previous models of SN 1987A (Wesson et al. 2015; Ercolano et al. 2007). Figures 10 to 12 show the best fits to the data for days 714 to 3604 and table 3 details the parameters used.

It can be seen that, in order to reproduce the blueshifts seen in the [OI] $\lambda 6300, 6363 \text{ \AA}$ doublet, considerably larger dust masses are required than to fit the H α line. However, larger maximum velocities are also required to fit the wings and a significantly steeper density profile is required. The inner radii remain approximately similar in both the H α and [OI] $\lambda 6300, 6363 \text{ \AA}$ models whilst the outer radii are significantly different. This may indicate why a greater dust mass is required in order to fit the [OI] doublet; the doublet traces the dust to a wider radius than the H α line.

5.2 Clumped Models of SN 1987A

It has been shown through the modelling of photometric data that when dust is assumed to have a clumped distribution the derived masses can be significantly larger than if the dust is distributed smoothly between the inner and outer radii. We present two sets of fits to the data based on the modelling used by W15. Each fit is derived from the smooth best fitting model such that the packets are emitted according to a smooth radial density profile. However, the dust is no longer coupled to the gas but instead is located entirely in clumps of size $R_{out}/30$. The clumps are distributed stochastically between R_{in} and R_{out} with the probability of a given grid cell being a clump proportional to $r^{-\beta}$ where $i(r) \propto r^{-2\beta}$. The number of clumps used is determined by the filling factor which is kept constant at $f = 0.1$. All properties are fixed from the smooth models with the exception of grain size and dust mass.

As for fully self-consistent radiative transfer models of photometric data, the dust masses required to reproduce the same degree of absorption in a clumped setting are considerably higher than in the smooth case. However, it also necessary to have a slightly larger albedo in order to reproduce the red side of the profiles. This is presumably because when the dust is located in clumps the radiation is subject to less scattering as well as less absorption. The reduction in scattering appears not to be compensated for by the increased dust mass and a larger grain size is therefore required, particularly at day 714. A grain size of $a = 0.6 \mu\text{m}$ is therefore used throughout the clumped models as the smallest possible grain size capable of reproducing the data reasonably. Full details of all parameters used for these models may be found in table 4 and the fits are presented in figures 13 to 15.

Since these models also utilise the smallest possible grain size and therefore represent an approximate minimum dust mass in the case of a clumped distribution of amorphous carbon, we also investigate the potential for this method to derive an upper bound on the dust mass. By steadily reducing the grain size from an initial value of $5 \mu\text{m}$ (motivated by the maximum possible grain size derived by W15 for their day 8515 model), we produce a set of models representing a theoretical maximal dust mass. Throughout the course of our modelling it transpired that the grain size used for the minimum models at days 714 and 806 ($a = 0.6 \mu\text{m}$) in fact represents the best fit to the data and even a small fluctuation in a in either direction results in a significantly poorer fit, either over- or underestimating the red wing and the trough in the doublet. We therefore conclude that the dust mass estimates produced at days 714 and 806 for a grain size of $a = 0.6 \mu\text{m}$ are strong estimators of the dust mass at this epoch. At later epochs however we find that equally good fits may be generated by substantially larger grains with $a = 3.5 \mu\text{m}$ (see figure 16). Details of the parameters used in these models presented in table 5.

5.3 The effect of a grain size distribution

It is important to consider the potential effect on the dust mass of modelling a grain size distribution instead of a single grain size. For a grain size distribution the overall extinction cross section, C_{ext} , at a given wavelength is calculated as

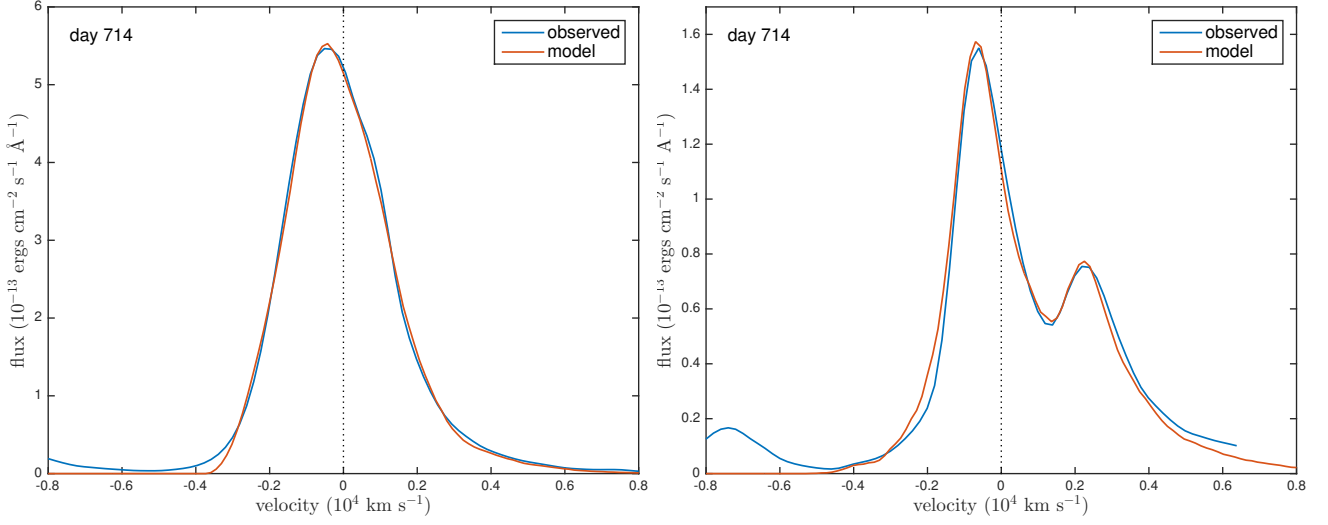


Figure 10. Best smooth fit to the day 714 H α line (left) and [OI] λ 6300,6363Å doublet (right) as per parameters detailed in table 3.

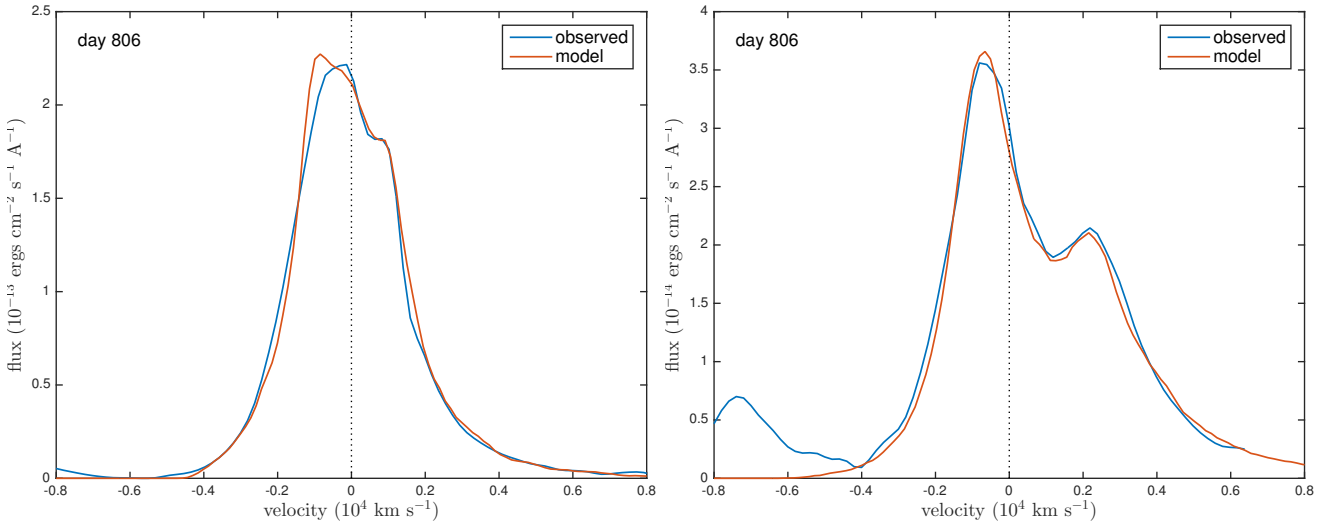


Figure 11. Best smooth fit to the day 806 H α line (left) and the [OI] λ 6300,6363Å doublet (right) as per parameters detailed in table 3.

Table 5. Details of the parameters used for the best fitting clumped models with $a = 3.5\mu\text{m}$.

day	v_{max} (kms $^{-1}$)	R_{in}/R_{out}	β	M_{dust} (M_{\odot})	a (μm)	R_{out} (cm)	R_{in} (cm)	$\tau_{H\alpha}$	τ_V	Figure No.
1862	8500	0.14	1.9	2.00E-02	3.50	1.37E+17	1.91E+16	0.85	1.70	16
2875	9500	0.12	2	8.00E-02	3.50	2.36E+17	2.83E+16	1.15	2.30	16
3604	10250	0.12	2	1.70E-01	3.50	3.19E+17	3.83E+16	1.33	2.67	16

$$C_{ext} = \int_{a_{min}}^{a_{max}} Q_{ext}(a) n(a) \pi a^2 da$$

where $Q_{ext}(a)$ is the extinction efficiency for a grain size a and $n(a)$ is the number of grains with size a . The overall extinction efficiency is then

$$Q_{ext} = \frac{C_{ext}}{\int_{a_{min}}^{a_{max}} n(a) \pi a^2 da}$$

The scattering cross-section Q_{sca} is similarly calculated. As a result of these calculations, there is rarely a single grain size that has the same albedo and extinction efficiency as a size distribution. Modelling a size distribution may therefore alter the deduced dust mass. Since the models are only sen-

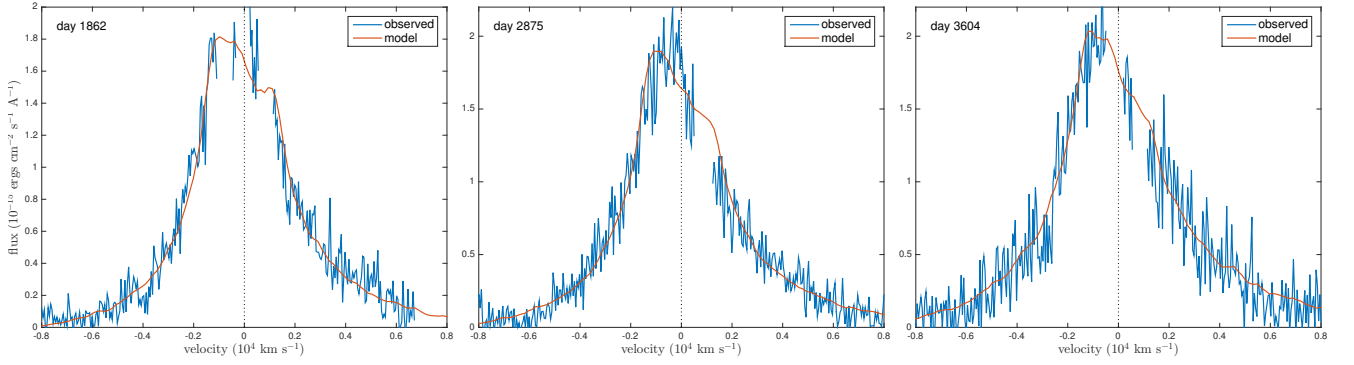


Figure 12. Best smooth fit to the H α line at days 1862, 2875 and 3604 as per parameters detailed in table 3.

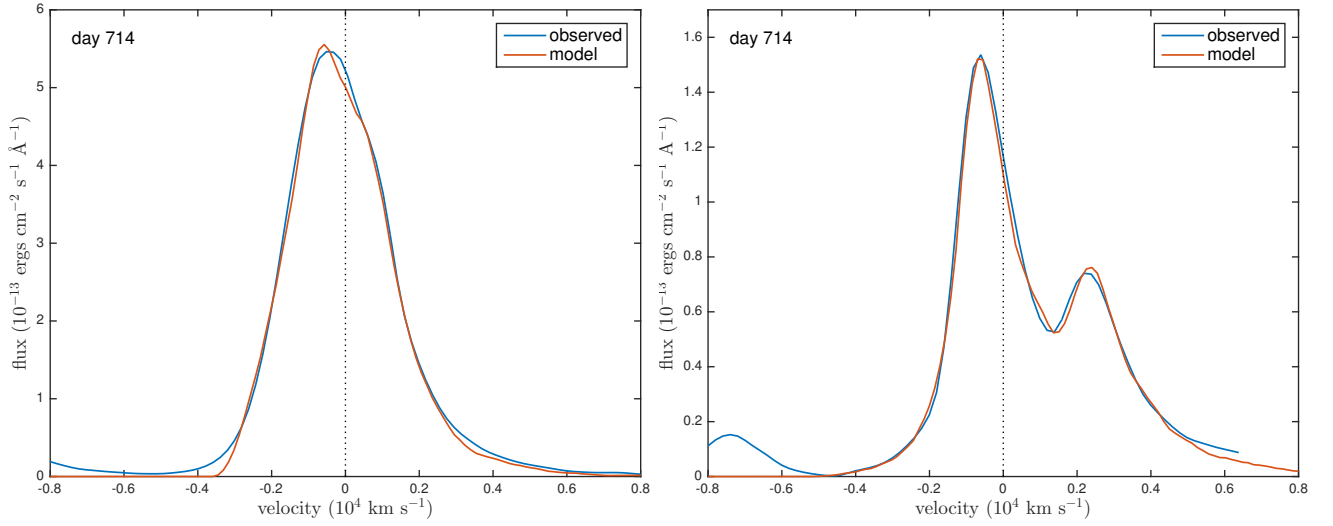


Figure 13. Best clumped fit to the day 714 H α line and [OI] λ 6300,6363Å doublet as per parameters detailed in table 4.

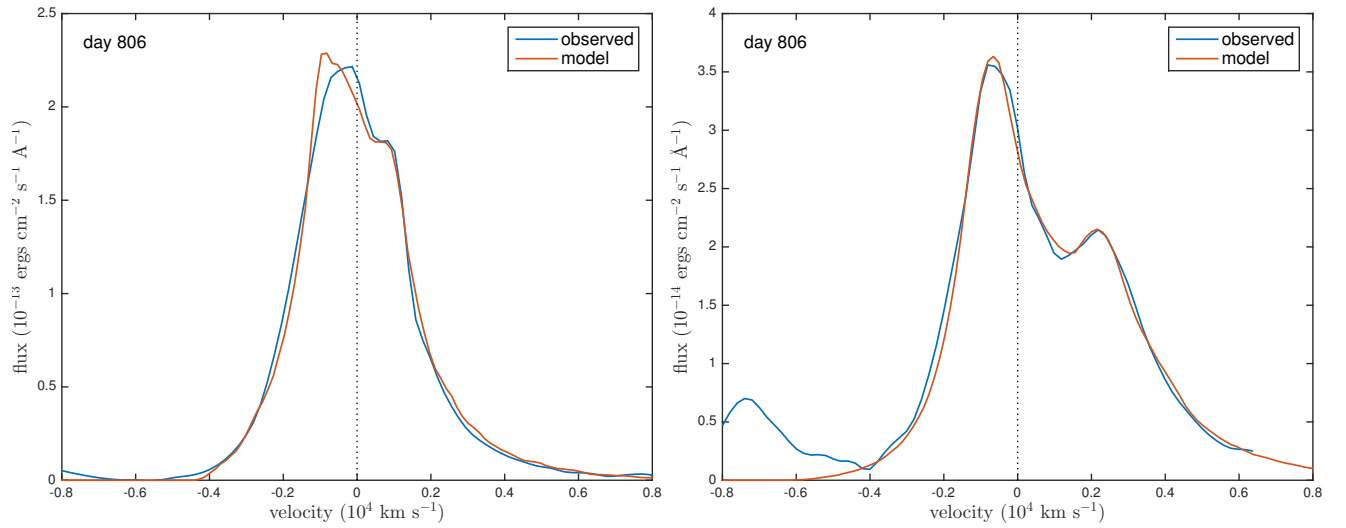


Figure 14. Best clumped fit to the day 806 H α line and [OI] λ 6300,6363Å doublet as per parameters detailed in table 4.

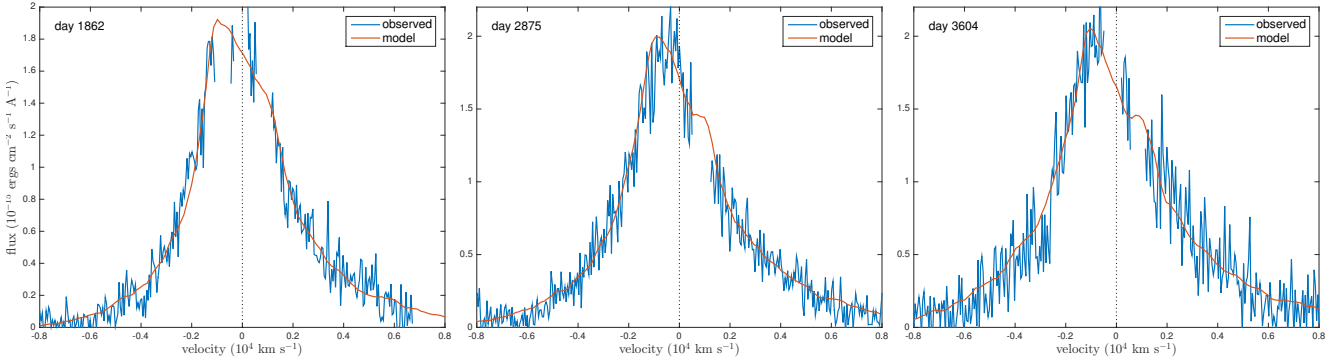


Figure 15. Best clumped fit to the H α line at days 1862, 2875 and 3604 as per parameters detailed in table 4 with $a = 0.6\mu\text{m}$.

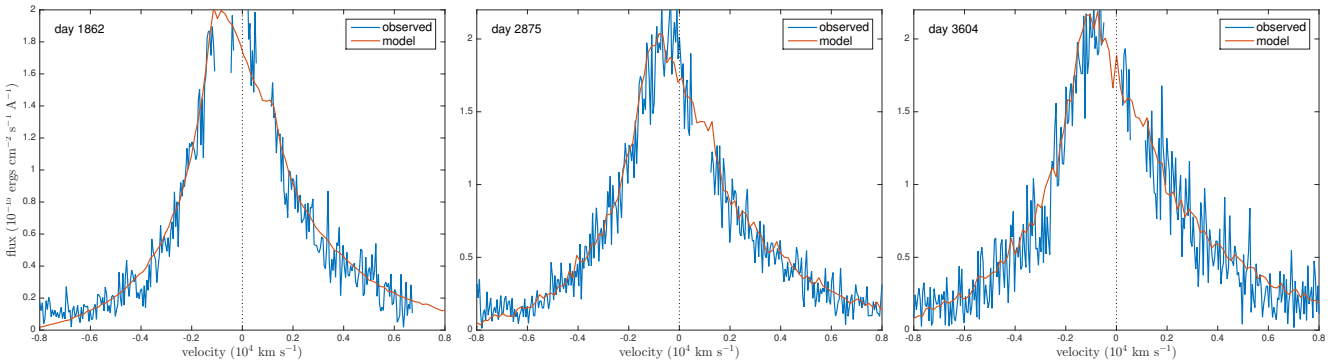


Figure 16. Best clumped fit to the H α line at days 1862, 2875 and 3604 as per parameters detailed in table 5 with $a = 3.5\mu\text{m}$.

sitive to the optical depth and the albedo, however, it is not possible to deduce the grain size range or distribution and only single grain sizes are investigated (as presented above).

Whilst this apparently limits the scope of the results, it is important to consider the extent to which considering grain size distributions would alter the derived dust masses. By considering a number of grain size ranges and adopting a power law distribution with a variable exponent, we may gain some insight into the effects of adopting a distribution rather than a single size. For the classical MRN power law ($n(a) \propto a^{-3.5}$) with a wide grain size range ($a_{\min} = 0.001\mu\text{m}$ to $a_{\max} = 4.0\mu\text{m}$) the derived albedo is much too small to reproduce the required wing seen at early epochs. We therefore adopt an approach whereby, for a number of grain size ranges, we adjust the exponent of the distribution until the overall albedo is the same as that seen for the best fitting single grain size for the clumped distributions. We may then approximately calculate the required dust mass as

$$M_d = \frac{M_s Q_{\text{ext},s}(a_s)}{a_s} \times \frac{\int_{a_{\min}}^{a_{\max}} n(a) a^3 da}{\int_{a_{\min}}^{a_{\max}} Q_{\text{ext}}(a) n(a) a^2 da} \quad (9)$$

where the subscript s represents the single grain size quantities and the d subscript represents quantities for the grain size distribution.

We calculate the required dust masses for the clumped model on day 714 for a selection of distributions with varied a_{\min} . These are presented in table 6. It can be seen that in all cases, a larger dust mass is required in order to

Table 6. Equivalent dust masses for the day 714 clumped models using grain size distributions and 100% amorphous carbon. f is factor of increase from the dust mass for the single size model ($M = 7 \times 10^{-5} M_{\odot}$ with $a = 0.6\mu\text{m}$) and p is the exponent of the grain size distribution $n(a) \propto a^{-p}$.

a_{\min} (μm)	a_{\max} (μm)	p	M (M_{\odot})	f
0.001	4	2.45	1.93E-04	2.76
0.01	4	2.45	1.93E-04	2.76
0.05	4	2.52	1.84E-04	2.62
0.1	4	2.72	1.61E-04	2.3
0.5	4	8.2	7.23E-04	1.03

reproduce the same conditions as a single grain size. The conversion factors presented in the table are valid for any model with grain size $a = 0.6\mu\text{m}$ and may therefore also be applied to the models for day 806. We repeated the process for $a = 3.5\mu\text{m}$ but found that, in order to reproduce the required albedo, the distribution had to be heavily weighted towards the larger grains and that the value of a_{\min} had no effect of the required dust mass. Increasing the value of a_{\min} to larger values ($> 2\mu\text{m}$) does not have a significant effect either. This is because both extinction efficiency and albedo tend to a constant value with increasing grain radius and the adoption of different grain size ranges and distributions above a certain threshold therefore results in only insignificant variation in these quantities.

This calculation in equation 9 holds only for a single wavelength and therefore is not exact for our models which

obviously transport radiation over a range of wavelengths. However, the dust masses derived using the above formula produce almost identical fits to the data as for the single grain size and therefore give an excellent suggestion of the approximate dust mass required when using a distribution.

We therefore conclude that, if a distribution of grain sizes is indeed present, the deduced dust masses are likely to be under-estimating the true mass of newly formed dust rather than overestimating it.

5.4 The effect of different species

In all of our analyses heretofore, we have considered only amorphous carbon as the species of interest. This is in part motivated by previously published literature that suggests that, if silicates do form a fraction of the total dust mass, it is likely that that fraction is limited to approximately 15% (W15, Ercolano et al. (2007)). It is also partly motivated by the nature of the model; the parameters that affect the quantity of dust required in the model are the albedo and the optical depth. There are likely many possible combinations of species and grain sizes that result in a good fit to the data.

We consider the change in dust mass when a medium of 100% silicates is used instead of amorphous carbon. We use optical constants presented in ?. In a similar manner to the approach detailed in section 5.3, we may calculate the mass of silicates that is equivalent to a carbon mass for a single grain size. We consider the albedo at the original grain size, calculate the equivalent grain size for silicates that results in the same albedo and then calculate the new dust mass by considering the change in the extinction efficiency as

$$M_{sil} = M_{amc} \left(\frac{Q_{amc}}{Q_{sil}} \right) \left(\frac{a_{sil}}{a_{amc}} \right) \left(\frac{\rho_{sil}}{\rho_{amc}} \right) \quad (10)$$

Because of the nature of the variation of albedo with grain size for silicates (see figure ??), there is often more than one silicate grain size that will give rise to the same albedo. We consider all the possibilities and the resulting mass conversion factors in table 7. In our best fitting models for days 714 and 806, using any fraction of silicates of either grain size would serve to increase the dust mass. However, at later epochs, using some fraction of silicate dust would reduce the dust mass to potentially more than half of our estimated values. However, this is still within our predicted range and our minimum and maximum dust masses remain robust.

5.5 Contamination of the the H α profiles at days 704 and 806

The profile at day 704 exhibits several of the features discussed above. There is an increase in flux on the red side of the data $v > 2000 \text{ km s}^{-1}$ as a result of a dust scattering reprocessing radiation to the red. There is also an approximately linear section between the peak at $v = -420 \text{ km s}^{-1}$ and the very slight corner visible at v_{min} . The profile at day 806 has similarly identifiable features with a noticeable wing on the red side extending out to $v = 8000 \text{ km s}^{-1}$. It also exhibits a definite shoulder reaching to $v \approx 900 \text{ km s}^{-1}$ which we assume to be the value of v_{min} . In both these

Table 7. Equivalent dust masses for the day 714 clumped models using grain size distributions and 100% amorphous carbon. f is factor of increase from the dust mass for the single size model ($M = 7 \times 10^{-5} M_{\odot}$ with $a = 0.6 \mu\text{m}$) and p is the exponent of the grain size distribution $n(a) \propto a^{-p}$.

carbon		silicates		$f = M_{sil}/M_{amc}$
a	Q_{ext}	a	Q_{ext}	
0.6	2.60633	0.0583	0.0772	5.37
0.6	2.60633	4	2.1828	13
3.5	2.2129	0.0641	0.10182	0.65
3.5	2.2129	1.02	2.149	0.49
3.5	2.2129	1.376	2.3514	0.61

cases, with both smooth and clumped models, we struggle slightly to fit both the corner and the peak of the profile. In both instances, accurately fitting the corner results in a peak that is slightly further towards the blue than is seen in the observations. We suggest that this discrepancy, which is more noticable at day 806 because of the more distinctive shape of the profile, is likely a result of the increased flux produced by the clump at $v = -360 \text{ km s}^{-1}$. This clump, clearly visible in the line profile at day 673 and identified as such in the literature (Spyromilio et al. 1993; Hanuschik et al. 1993), is likely contaminating the position of the peaks of the profiles at days 714 and 806. The clump is perhaps not so clearly discernible at these epochs as a result of the poor resolution of the CTIO spectra but is known to persist until around day 900 (Hanuschik et al. 1993).

5.6 The shoulder in the H α line profile at day 806

The shoulder in the H α line profile at day 806 has previously been attributed to an unresolved [NII] $\lambda 6583\text{\AA}$ line at $v = 933 \text{ km s}^{-1}$ (?). Narrow [NII] lines at $\lambda = 6583\text{\AA}$ and $\lambda = 6548\text{\AA}$ are certainly seen by day 1862 and have to be removed in order to consider the evolution of the broad H α profile. It is somewhat unfortunate that the theoretical minimum velocity falls at a similar velocity to this line as it makes it difficult to distinguish the two features. We postulate however that this feature may in fact be a product of a relatively steep density profile and the formation of dust within the ejecta as demonstrated in both our fits (see figures 11 and 14) and our investigation of the parameter space (see figures 5 and 6).

It is a general challenge inherent in the nature of this modelling that interesting features that are present in line profiles are not necessarily easily identifiable. In particular, the effects of clumping and asymmetrical distributions in the ejecta may cause fluctuations that are hard to distinguish from the potential signatures of dust formation discussed in section 4. Key indicators such as symmetry in the location of discontinuities on the red and blue side, typical dust profile signatures and the presence of a red scattering wing should be considered.

5.7 Potential challenges at later epochs: days 1862, 2875 and 3604

At later epochs, even very tiny fluctuations in adopted value of the continuum level can have a substantial effect on the fit of the resulting profile. Since it is not feasible to establish the level of the continuum so precisely, the value of the continuum has been left as a free parameter that may be adjusted (to within sensible margins) in order to allow for the widest possible dust mass range to be determined. We generally find it is necessary to assume a continuum level that is slightly lower where the adopted dust mass is higher.

The line profiles at these later epochs are relatively noisy and have had substantial sections of the profile removed as a result of contamination by the $H\alpha$ and $[NII]$ narrow lines. Unfortunately, this removes a critical section of the line ($500 \text{ km s}^{-1} < v < 1500 \text{ km s}^{-1}$) that would be potentially informative. However, we do achieve excellent fits to the line profiles at these epochs.

6 DISCUSSION

We have collated a range of archival spectral data in the optical and IR and, by modelling the evolution of the $H\alpha$ and $[OI]\lambda 6300, 6363\text{\AA}$ lines, have placed constraints on the evolution of newly formed dust in SN 1987A. We have done this using Monte Carlo models that consider both the absorbing and scattering effects of dust. We find dust masses that are in excellent agreement with those previously found at similar epochs. We obtain large dust masses at just a few thousand days in agreement with the very large mass of dust deduced by *mikako ref problem* from their observations at long wavelengths using Herschel. We compare our dust masses directly with those obtained by W15 in order to compare both their magnitude and evolution (see figure 17).

At all epochs we find that we obtain slightly smaller dust masses than those of W15 although our values are still generally within the error bars placed on their values. There may be a number of different reasons for this. Firstly, our modelling is somewhat more conservative in its estimates since we use an environment of pure amorphous carbon whereas the models presented by W15 use a silicate fraction of 0.15 which is likely to increase the overall mass of dust required to produce the same observations, both in the case of radiative transfer SED modelling and line profile modelling. Secondly, we use different sets of optical constants; we have used the optical constants derive by Zubko et al. (1996) from their BE sample where W15 use constants from *?hanner ref problem*. They state that in order to fit their data at early epochs (day 615) with the Zubko ACH2 sample smaller inner and outer radii are needed and half as much dust ($5.0 \times 10^{-4} M_{\odot}$) is required. This is considerably closer to the values we derive at similar epochs.

The other significant difference between our models is the adopted grain size distribution. W15 generate fits to their early data using an MRN distribution between $0.005\mu\text{m}$ and $0.25\mu\text{m}$ in size. They cannot obtain a fit with grains of $\sim 1.0\mu\text{m}$ in size at early epochs. However, they do not consider values in between these size point as we conclude is likely the case with grain sizes of $a \approx 0.6\mu\text{m}$. For SED modelling

it is generally the case that the larger the grain size used, the less dust is required to produce the same level of flux and it may therefore be this difference that is generating the discrepancy in our results. W15 use this property to derive a maximum possible grain size at late epochs as well and conclude that grains cannot be larger than $\sim 5\mu\text{m}$ by day 8515. This is directly in line with the maximum grain sizes we derive at slightly earlier epochs. We find that the grain size likely cannot have exceeded $\sim 3.5\mu\text{m}$ at day 3604 and the dust masses that we generate using this value are very similar to the value of the W15 sigmoid fit at this epoch.

Determining the relationship between the size of dust grains in the ejecta and the time post-explosion is important for understanding the likelihood of dust surviving the passage of the reverse shock travelling back through the ejecta. By the time the reverse shock begins to appear in the line profiles (around day 5000), our models predict that the grains could already be as large as several microns in radius but are certainly larger than $\sim 0.6\mu\text{m}$. Grains larger than $\sim 0.2\mu\text{m}$ are likely to survive and thus the majority of the dust produced is likely to survive (remembering that our modelling only considers an average grain size and makes no comment about the grain size distribution). It has recently been suggested that very large grains (up to $4.2\mu\text{m}$) may have formed in the ejecta of SN 2010jl very soon after the explosion (a few hundred days) Gall et al. (2014). Whilst the values we suggest are not as high that postulated by Gall et al. (2014), they maintain a distribution that remains steeped towards the smaller end of the scale and thus, as our models only treat a single, average grain size, these values may be not be at odds. Certainly, both results suggest that grains large enough to survive the destructive force of the reverse shock have formed by a few hundred days post-explosion.

There is now a firm consensus that a very large quantity of dust has formed in SN 1987A between the time of the original explosion and the present day. Perhaps more important therefore is the manner of its evolution. We have shown that dust masses have reached the order of $0.1M_{\odot}$ by day 3604. However, it is known that values several times as large as this are ultimately expected and thus a substantial fraction of the dust is likely to form after this epoch. This is in strong agreement with the results produced by W15. They derive a sigmoid fit to their dust mass evolution of the form

$$M_d(t) = ae^{be^ct}$$

where they obtain values of $a = 1.0M_{\odot}$ (representing the maximum dust mass), $b = -8.53$ and $c = -0.000366$. Both their dust masses and this sigmoid fit are shown in figure 17. This exhibits an initial period of slow growth followed by an intermediary period of acceleration followed by another slowing until a plateau is ultimately reached. In this sense it may be relatively representative of the process of dust formation whereby initial conditions appropriate for grain growth gradually develop until optimal conditions are reached at an intermediate epoch when grain growth is at its fastest before conditions once again deteriorate and the rate slows again (as discussed by W15). Performing a least-squares regression to this function using our predicted dust masses, we derive a sigmoid fit with coefficients $a = 0.58M_{\odot}$,

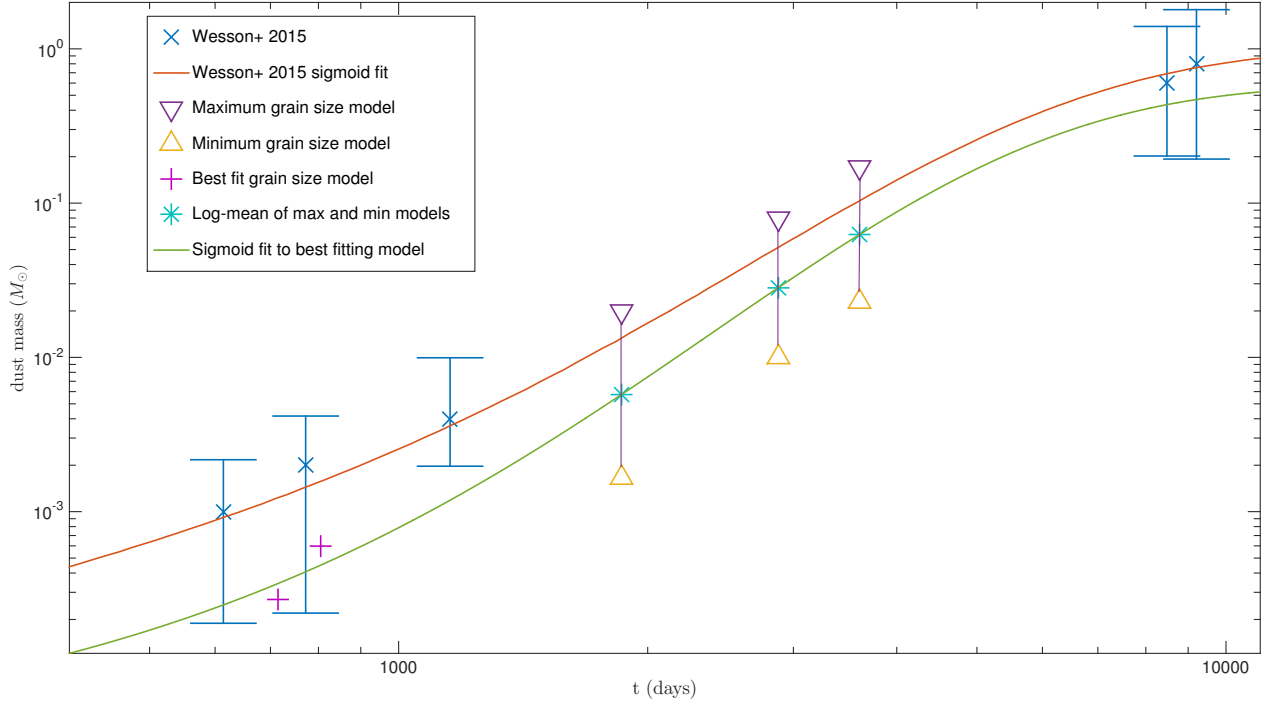


Figure 17. Purple and yellow triangles - Maximum ($a = 3.5\mu\text{m}$) and minimum ($a = 0.6\mu\text{m}$) dust masses respectively. Values are from the later epoch ($t > 1862$ days) clumped models of $\text{H}\alpha$. Pink crosses - Predicted dust masses (clumped models of the $[\text{OI}]\lambda 6300, 6363\text{\AA}$ doublet with grain size $a = 0.6\mu\text{m}$). Turquoise stars - Predicted dust masses calculated as a log average of the maximum and minimum values. Green - Sigmoid fit to our predicted dust masses. Blue - dust masses derived by W15 in their photometric modelling of SN 1987A. Red - sigmoid fit to the W15 values.

$b = -10.02$ and $c = -0.000416$. These values are remarkably similar to those derived by W15 although the final predicted dust mass is slightly smaller in our case. This sigmoid fit is also plotted in figure 17.

Our modelling concurs with the suggestion of W15 that even after ~ 3000 days the dust mass is only a very small fraction of its final value. This is in contrast to Sarangi & Cherchne (2015) whose chemistry models predict that the evolution of dust formation will have reached its plateau by around 5 years after the explosion first occurred.

Ideally, our models would cover the entire evolution of SN 1987A right up to the present day. However, the excitation of gas in the outer edges of the ejecta by the reverse shock after \sim day 500 results in a significant, broad and asymmetric flux that dominates the original line profile. In addition to this, the narrow lines from the ring start to become so significant relative to the original broad $\text{H}\alpha$ profile that, post-removal, there is not enough of the broad profile remaining to be able reliably infer information from its features. These are factors that are likely to be common to most core collapse supernovae and thus are likely to have an impact on the wider applicability of this particular technique at later epochs. Care should also be taken in the future to ensure that the line profiles are the temporally appropriate profile and not in fact a product of a light echo representing the state of the ejecta at some previous epoch. Nonetheless, this technique has proved effective in determin-

ing dust masses formed in core-collapse supernovae through the detailed modelling of asymmetric line profiles and clearly has wider application to multiple supernovae and supernova remnants.

7 CONCLUSIONS

We have discussed in section 4 the various potential effects of dust scattering and absorption on the generic shape of a line profile and the different features that may be produced. In particular, attention should be paid to the fact that the classical blue-shifted peak and asymmetric profile with most flux on the blue side is very much not the only profile that signifies the presence of dust. Profiles may also have the majority of their flux on the red side in the case of strong scatterers. They will often exhibit an extended red scattering wing although care should be taken to first ascertain that this cannot be accounted for by electron scattering. It is feasible that a pronounced shoulder or corner may be present on the red side of the profile located at the minimum velocity of the shell. This feature may often be mistaken for a narrow line, a product of a lack of resolution or a geometrical effect.

We have modelled $\text{H}\alpha$ and $[\text{OI}]\lambda 6300, 6363\text{\AA}$ line profiles from SN 1987A over a range of epochs and obtained dust masses of the order of $0.1M_{\odot}$ by day 3604. We derive a sigmoid fit to this data that predicts a final dust mass

of $0.68M_{\odot}$ in line with both other predictions and current dust mass estimates for SN 1987A. We conclude that large grains are necessary in order to reproduce the extended red scattering wing and asymmetry seen in several of the lines and that grains larger than $0.6\mu\text{m}$ have formed by day 604.

We have demonstrated the efficacy of the DAMOCLES code for determining dust masses and established its potential for application to other supernovae and spectra, both archival and current.

ACKNOWLEDGMENTS

The authors would like to thank Dr Jeremy Yates for discussion and guidance throughout the development of the DAMOCLES code. We would also like to thank Dr Rayley Stathakis for providing us with the AAT data. This work has been made possible by the Science and Technology Facilities Council. *ArchiveReferences*

REFERENCES

- Auer L., Blerkom D. V., 1972, *Astrophys. J.*
 Barlow M. J., et al., 2010, *Astron. Astrophys.*, 518, L138
 Chugai N. N., Chevalier R. a., Kirshner R. P., Challis P. M., 1997, *Astrophys. J.*, 483, 925
 Ercolano B., Barlow M. J., Sugerman B. E. K., 2007, *Mon. Not. R. Astron. Soc.*, 375, 753
 Fransson C., Ergon M., Challis P., 2013, arXiv Prepr. arXiv ...
 Gall C., et al., 2014, *Nature*, 511, 326
 Gerasimovic B., 1933, *Zeitschrift für Astrophys.*, 7, 335
 Gomez H. L., et al., 2012, *Mon. Not. R. Astron. Soc.*, 420, 3557
 Gröningsson P., Fransson C., Lundqvist P., Nymark T., Lundqvist N., Chevalier R., Leibundgut B., Spyromilio J., 2006, *Astron. Astrophys.*, 5325, 11
 Gröningsson P., et al., 2007, *Astron. Astrophys.*, 491, 19
 Gröningsson P., et al., 2008, *Astron. Astrophys.*, 479, 761
 Hanuschik R. W., Spyromilio J., Stathakis R., Kimeswenger S., Gochermann J., Seidensticker K. J., Meurer G., 1993, *Mon. Not. R. Astron. Soc.*, 261, 909
 Hillier ., 1991, *Astron. Astrophys.* (ISSN 0004-6361), 247, 455
 Lucy L., Danziger I., Gouffes C., Bouchet P., 1989, *Struct. Dyn.* ..., pp 164–179
 Owen P. J., Barlow M. J., 2015, *Astrophys. J.*, 801, 141
 Phillips M. M., Hamuy M., Heathcote S. R., Suntzeff N. B., Kirhakos S., 1990, An optical spectrophotometric atlas of supernova 1987A in the LMC. II - CCD observations from day 198 to 805, [doi:10.1086/115402](https://doi.org/10.1086/115402)
 Sarangi A., Cherchne I., 2015, pp 1–20
 Smith N., Silverman J. M., Filippenko A. V., Cooper M. C., Matheson T., Bian F., Weiner B. J., Comerford J. M., 2012, *Astron. J.*, 17, 6
 Spyromilio J., Stathakis R., Cannon R., Waterman L., Couch W., Dopita M., 1991, *Mon. Not. R. Astron. Soc.*, 248, 465
 Spyromilio J., Stathakis R. a., Meurer G. R., 1993, *Mon. Not. R. Astron. Soc.*, 263, 530
 Tziamtzis a., Lundqvist P., Gröningsson P., Nasoudi-Shoar S., 2010, *Astron. Astrophys.*, 35, 15
 Wang L., et al., 1996, *Astrophys. J.*, p. 26
 Wesson R., Barlow M. J., Matsuura M., Ercolano B., 2015, *Mon. Not. R. Astron. Soc.*, 446, 2089
 Zubko V. G., Mennella V., Colangeli L., Bussolletti E., 1996, *Mon. Not. R. Astron. Soc. Lett.*, 282, 1321

APPENDIX A: APPENDIX A

Since the outflow velocities in supernovae are high, the photon packets are subject to Doppler shifting at emission and at each scattering event. When the packet is initially emitted, it has a frequency and a trajectory in the rest frame of the emitter. Both of these must be transformed to the observer's frame in order for the packet to be propagated through the grid. The new direction and frequency in the observer's frame may be simply found by transforming the momentum 4-vector \mathbf{P} which is defined as

$$\mathbf{P} = \begin{pmatrix} E \\ p_x \\ p_y \\ p_z \end{pmatrix} = \begin{pmatrix} h\nu \\ h\nu x \\ h\nu y \\ h\nu z \end{pmatrix} \quad (\text{A1})$$

We may then derive \mathbf{P}' , the momentum 4-vector in the observer's frame using the relation

$$\mathbf{P}' = \Lambda \mathbf{P} \quad (\text{A2})$$

where

$$\Lambda = \begin{pmatrix} \gamma & -\gamma\beta_x & -\gamma\beta_y & -\gamma\beta_z \\ -\gamma\beta_x & 1 + (\gamma - 1)\frac{\beta_x^2}{\beta^2} & (\gamma - 1)\frac{\beta_x\beta_y}{\beta^2} & (\gamma - 1)\frac{\beta_x\beta_z}{\beta^2} \\ -\gamma\beta_y & (\gamma - 1)\frac{\beta_y\beta_x}{\beta^2} & 1 + (\gamma - 1)\frac{\beta_y^2}{\beta^2} & (\gamma - 1)\frac{\beta_y\beta_z}{\beta^2} \\ -\gamma\beta_z & (\gamma - 1)\frac{\beta_z\beta_x}{\beta^2} & (\gamma - 1)\frac{\beta_z\beta_y}{\beta^2} & 1 + (\gamma - 1)\frac{\beta_z^2}{\beta^2} \end{pmatrix}$$

and $\beta = \frac{v}{c}$, $\beta = (\beta_x, \beta_y, \beta_z)$, $\beta = \beta$ and $\gamma = \frac{1}{\sqrt{1 - \beta^2}}$.

In practice, the velocities considered are low enough that it is unnecessary to consider terms of order $O(\frac{v^2}{c^2})$ and thus Λ may be reduced to

$$\Lambda = \begin{pmatrix} 1 & -\beta_x & -\beta_y & -\beta_z \\ -\beta_x & 1 & 0 & 0 \\ -\beta_y & 0 & 1 & 0 \\ -\beta_z & 0 & 0 & 1 \end{pmatrix} \quad (\text{A3})$$

The new direction of travel and frequency in the observer's frame are therefore given by

$$\nu' = \nu(1 - x\beta_x - y\beta_y - z\beta_z) \quad (\text{A4})$$

$$x' = \frac{\nu}{\nu'}(x - \beta_x)$$

$$y' = \frac{\nu}{\nu'}(y - \beta_y)$$

$$z' = \frac{\nu}{\nu'}(z - \beta_z)$$

For each scattering event, the packet must be transformed both into and out of the comoving frame. The reverse transform is applied by using the inverse Lorentz matrix Λ^{-1} which is obtained by reversing the sign of \mathbf{v} . Positive \mathbf{v} is defined for frames moving away from each other and thus \mathbf{v} is defined to be negative in the direction of the observer.

This paper has been typeset from a \LaTeX file prepared by the author.